TURUN
YLIOPISTO
UNIVERSITY
OF TURKU

Quantifying General and Special Relativistic Contributions to Observed Polarization in Black Hole Accretion Disks Using Exact Analytical Formulae

---

Aiman Hanif

University of Turku
Faculty of Science and Engineering
Department of Physics and Astronomy
Master's Programme in Physical and Chemical Sciences
Theoretical Physics

Supervised by
Dr. Alexandra Veledina
Department of Physics and Astronomy
University of Turku

Turku, Finland
December 2025

UNIVERSITY OF TURKU

Faculty of Science and Engineering
Department of Physics and Astronomy
Theoretical Physics
Master's Programme in Physical and Chemical Sciences
AIMAN HANIF: Quantifying General and Special Relativistic Contributions to Observed Polarization in Black Hole Accretion Disks Using Exact Analytical Formulae
Master's Thesis, 43 pp.
December 2025

Abstract

Accretion disk polarimetry provides a valuable probe of the strong gravity region surrounding black holes. However, the physical origin and geometric dependence of X-ray polarization signatures in black hole X-ray binaries are still not fully understood. In this work, an analytical study of polarization from accretion disks around a Schwarzschild black hole is presented, with application to the well-studied system Cygnus X-1. The analysis adopts the analytical framework developed by Loktev et al.[27], which yields explicit expressions for the rotation of the polarization plane and accurately incorporates gravitational light bending and relativistic aberration without relying on computationally expensive ray-tracing techniques. Polarimetric maps are produced for observer inclinations of 30°, 50°, and 75° to illustrate how strong gravitational effects modify the observed polarization patterns. The assumptions of the model, including optically thick, plane-parallel disk emission and purely azimuthal gas motion, are discussed in detail. While real accretion flows may exhibit optically thin regions, radial velocity components, non-aligned magnetic fields, and localized emission from hot spots, the results demonstrate that polarization signatures remain highly sensitive to viewing geometry. This study provides useful insight for interpreting current and future X-ray polarimetric observations of black hole systems, particularly from missions like IXPE (Imaging X-ray Polarimetry Explorer). The methodology presented here offers an efficient computational approach that can be applied to analyze polarimetric data from various black hole systems, contributing to our understanding of accretion physics and strong-field general relativity.

KEYWORDS: Black holes, accretion disks, X-ray polarimetry, general relativity, Cygnus X-1, IXPE, Schwarzschild metric, relativistic effects

Contents

Abbreviations

ADAF	Advection-Dominated Accretion Flow
ADC	Accretion Disc Corona
AGN	Active Galactic Nucleus (Nuclei)
BH	Black Hole
BHB	Black Hole Binary
BHXR	Black Hole X-ray Binary
EHT	Event Horizon Telescope
GR	General Relativity
GRMHD	General Relativistic Magnetohydrodynamics
HEXTE	High Energy X-ray Timing Experiment
HMXB	High Mass X-ray Binary
INTEGRAL	International Gamma-Ray Astrophysics Laboratory
ISCO	Innermost Stable Circular Orbit
IXPE	Imaging X-ray Polarimetry Explorer
LHAF	Luminous Hot Accretion Flow
LMXB	Low Mass X-ray Binary
MRI	Magneto-Rotational Instability
NS	Neutron Star
OSSE	Oriented Scintillation Spectrometer Experiment
PA	Polarization Angle
PCA	Proportional Counter Array
PD	Polarization Degree
PoGO+	Polarized Gamma-ray Observer Plus
QPO	Quasi-Periodic Oscillation
RXTE	Rossi X-ray Timing Explorer
SED	Spectral Energy Distribution
SR	Special Relativity

1 Introduction

1.1 Understanding of accretion disk

Black Holes are considered essential tools for a much deeper understanding of important concepts in physics and for testing Einstein's theory of relativity. Black holes are also necessary for the evolution of galaxies. Accreting matter that falls into black holes prevents gas from cooling and forming stars, directly impacting the star formation rate in a galaxy. When the universe was 20 percent of its current age, galaxies were merging, causing supermassive black holes to coalesce into more massive black holes. This merging of galaxies provided these supermassive black holes with more gas, dust, and matter. As a result, black holes begin to accrete matter and become active, which is why at around $z \sim 2$, Quasars (one of the brightest types of AGN) and star formation were at their peak, suggesting that both black holes and galaxies grow together. At the beginning of the universe, X-rays from black holes also helped in the process of reionization.

New advances in X-ray and radio telescopes have improved our understanding of how accretion flows and jets are connected, which led us to come up with better models that explain the wide variety of spectra and variability patterns like QPOS observed in BH and NS.

The behavior of a steady BH depends on its Mass, spin, and inclination angle, or any variability over time. Finding mass and inclination in a binary system is easy. However, spin causes a disruption in the spacetime around the BH, which makes it harder to measure spin and mass accretion rate. Mass accretion rate is even trickier to measure because it depends on both spin and accretion rate flow at the horizon. X-ray luminosity cannot measure the mass accretion rate either, because not all energy is radiated away: some of it is carried away into the BH or lost in jets and winds.

In the standard model [23],we ignore jets, winds, and the advection process, and we simply assume that heat radiates away locally. The accretion disk also behaves like a quasi-blackbody, where $T(r) \propto r^{-3/4}$, in this model, which means the inner disk has higher pressure compared to the outer disk. In this model, matter that falls into the BH produces friction between particles in the disk and converts K.E. into heat. The formula for this viscous stress according to Shakura Sunyaev model is $t_{r\phi} = \alpha P_{\rm tot}$ where $P_{\rm tot} = P_{\rm gas} + P_{\rm rad}$. One of the main breakthroughs was identifying the cause of this viscous stress, which turned out to be the magneto-rotational instability (MRI). After this major discovery, many simulations were proposed and are still being developed, and they have already proven helpful in understanding jets and accretion flow.

The accretion disk in Shakura Sunyaev model [23] is steady, but in reality, it can become unstable because of two main reasons: hydrogen ionization at low luminosities (thermal-viscous instability) and radiation pressure at high luminosities (radiation-pressure instability).

When the disk becomes unstable due to a slight increase in temperature, causing hydrogen ionization, which increases opacity and further raises the temperature and ionization, this is known as thermal instability. Similarly, if a slight increase in temperature increases the mass accretion rate, which further triggers more accretion flow, resulting in depletion of the disc at that location, then it is known as viscous instability.

In a thin disc, $H/R \ll 1$, thermal instability is much faster than viscous instability, as shown in Fig. 1, which means the temperature in discs increases at a much faster rate before the disk even has a chance to redistribute its mass. On the contrary, for $H/R \gg 1$, both viscous and thermal instability happen at an equal rate, which allows the disk´s structure to adjust according to the increase in temperature. For example, at low mass accretion rates, the Shakura Sunyaev model becomes unstable around 10^4–10^5 K [23].

In the quiescent state, the temperature is too low to ionize hydrogen significantly, so the material stays mostly neutral, and thus, opacity is also low. As the temperature increases, opacity also rises, trapping more energy in the disk and heating it, thereby increasing ionization. This continues until all the hydrogen atoms are fully ionized, at which point the opacity curve becomes flat and thermal runaway stops.

How fast these instabilities grow depends on the timescale. The thermal timescale is

$$t_{\text{th}} \sim \alpha^{-1} t_{\text{dyn}}, \tag{1}$$

and the viscous timescale is

$$t_{\text{visc}} \sim \alpha^{-1} \left(\frac{H}{R} \right)^{-2} t_{\text{dyn}}, \tag{2}$$

where H is the vertical height of the disc, R is the radius, and t_{dyn} is the orbital timescale.

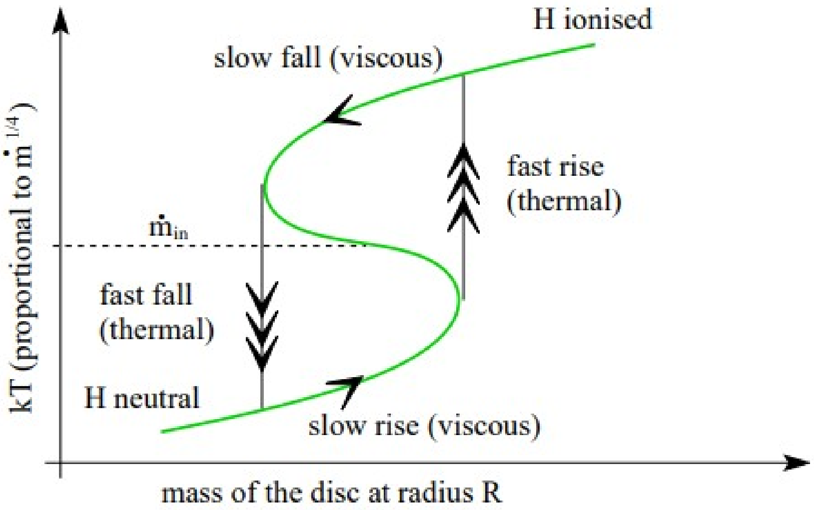

Figure 1: The thermal ionization instability. The figure shows the local effect of the instability, where hydrogen undergoes discontinuous ionization transitions at a given radius in the disc[7].

A small-scale instability in the accretion disk triggers a viscous instability. As the temperature increases at any local point, more and more hydrogen starts to ionize, the pressure starts to increase, and according to $\tau_{r\phi} = \alpha P$ [23], with increasing pressure, the viscous stress also increases, which causes the accretion mass flow to increase as well. The disk matter at that local point begins to deplete, and pressure starts to drop. The drop in pressure results in a drop in temperature, hydrogen recombines, and the disk begins to cool. This triggers a cooling instability. The disk is gradually filled up due to the inflow from the companion star, and the cycle continues.

This instability, which started locally, can spread quickly. At any unstable radius, a sudden change in temperature impacts the nearby region. If the contrast between these ionized and cooler states is sufficiently large, instability can grow throughout the disk, and the entire disk oscillates between hot and cold states. In this case, the hot state is the outburst phase, in which elevated temperature and viscosity generate heat waves that propagate throughout the disk, thereby maintaining a high accretion disk. While a colder state is quiescent, when the outer disk falls below the hydrogen ionization threshold, a cooling wave propagates throughout the disk, and the disk switches to the cold state.

Magneto-rotational instability (MRI) transports angular momentum from the inner gas to the outer gas. During the quiescent period, There aren´t many free electrons for the Magneto-rotational instability (MRI). SO, other insufficient processes, Such as hydrodynamic turbulence or spiral density wave, occur in the disk. Supermassive black holes act differently; they have lower densities and different chemical compositions. They have enough free electrons for MRI to persist and continue functioning even when the disk temperature is less than the hydrogen ionization threshold, which helps the disc to stabilize and prevent global outbursts.

While in a compact binary disc, MRI shows unique behavior. In white dwarfs, the MRI gets weaker or shuts off when the disk cools off, and transport drops sharply, but it switches back quickly when the disk becomes hotter. In Neutron stars (NS) and Black hole binaries (BHBs), the disc stability also depends on irradiation. High luminosity coming from the inner disk heats up the outer disk and keeps it above the hydrogen ionization threshold. As irradiation weakens, a cooling front develops and quickly stops the outburst. Systems that have longer orbital period and a large disc never fully ionize, and outbursts are less likely to occur in such systems.

Hence, while hydrogen instability gives a compelling explanation for the general observed disc outburst, overall, an accretion disk behavior is totally dependent on its local physics, the presence of irradiation, and the dominant angular momentum transport mechanism.

Light from the inner parts of the accretion disc doesn't reach the outer parts because the disc is usually shaped as a convex surface. To solve this problem, the Accretion Disc Corona (ADC) was proposed. It's a hot, thin material around the disc that can catch some X-rays and scatter them down onto the outer disc. In other words, it´s a large extended corona, and unlike a compact, Small Corona in Black holes and Neutron Stars, it is part of larger outflows and winds from the outer disk.

Irradiation not only explains extra light but also plays a key role in keeping the disc stable. Systems with massive companions known as High Mass X-ray binaries (HMXBs) like Cyg X-1 have high mass transfer rates, which keep the outer disc hot enough to avoid hydrogen ionization instability. Even though these systems have larger discs (because their orbits are larger), the high mass inflow more than compensates for it. That´s why HMXBs like Cyg X-1 tend to be more persistent, always active sources. In contrast, Low X-ray binaries (LXMBs) with black holes usually have lower mass transfer rates and cooler outer discs, which makes them more likely to go through cycles of outburst and quiescence. The models also help us understand why LXMBs with neutron stars are often more stable than those with black holes.

Neutron stars have less mass than black holes, so for the companion star to fill its Roche lobe, the system must have a smaller orbit. A smaller orbit means a smaller disc; a smaller disc stays warmer, so it is less likely to dip below the temperature at which hydrogen becomes neutral and causes instability. As a result, many neutron stars and LMXBs are persistent, although there are still some transient cases. Neutron star transients often have either large discs or extremely small discs (as in millisecond pulsars), where even a small drop in temperature can trigger an instability. Even though this Shakura Sunyaev [23] model explains a lot, the actual light curves of these systems can be quite complex. Some persistent systems show variability in their accretion disk even when they aren´t going into full outburst or are in quiescence. Long-period systems, especially, can show very strange outburst shapes, which are not simply a rise and decay. It is likely that a mix of effects, including irradiation, mass transfer changes from the companion, and tidal forces in the disk, is working together to produce this complex, diverse light curve behavior. Still, the overall match between theory and observation supports the idea that irradiated Shakura–Sunyaev type disk, regulated by hydrogen ionization instability, form the foundation for understanding accretion disks in these systems[23].

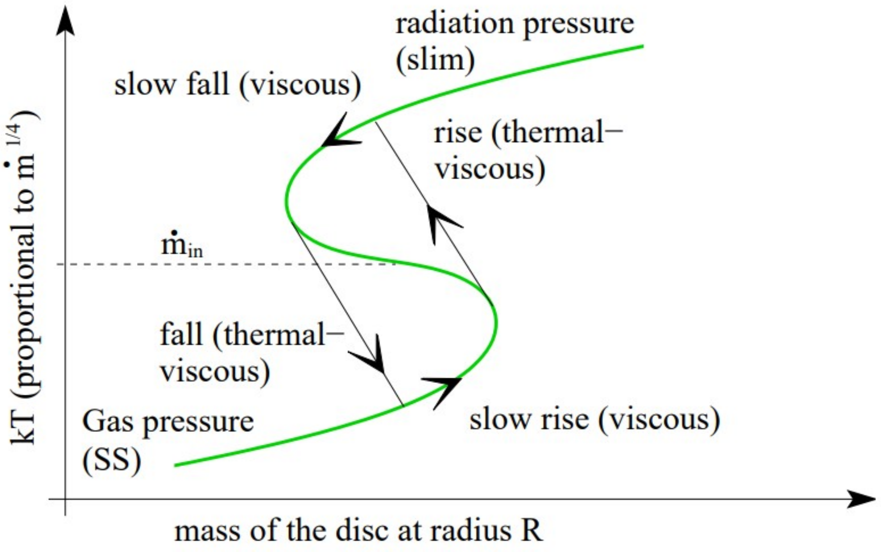

Figure 2: The radiation pressure instability. The figure shows the local effect of the instability, where the mass accretion rate through the disc jumps discontinuously at a given radius[7].

At high mass accretion rates, the inner regions of a Shakura–Sunyaev disc can be become unstable because of the transition from gas pressure dominance to radiation pressure dominance. In this case, a small increase in temperature can cause a bigger increase in pressure due to radiation, leading to stronger viscous stresses and more heating, which results in runaway heating, as there is no mechanism for processes (such as a drop in opacity) to enhance cooling. In the original Shakura-Sunyaev model[23], this instability lacks a high temperature and high accretion rate, so it predicts that the disc completely breaks down. However, adding radial advection introduces an additional cooling mechanism, where some energy is carried inward with the flow instead of radiating away immediately. This can restore stability similar to hydrogen ionization stability, but the difference is that the disc ($H/R \sim 1$) is thicker in this case, which results in viscous and thermal time scales to become similar; also, the MRI is the same across both gas and radiation-dominated cases. Despite theoretical predictions, there is little observational evidence of this radiation pressure instability.

The disc is expected to be unstable at around 6 percent of the Eddington luminosity, but in practice, it remains stable up to 70 percent of the Eddington luminosity, in black hole binaries, indicating that the Shakura–Sunyaev prescription might be incorrect [23]. An alternative approach that seems to match observation better, especially in very luminous sources like GRS 1915+105, is that stress scales with the geometric mean of gas and total pressure, which results in stability around 30 percent Eddington luminosity but remains globally stable due to energy transfer between neighboring disc regions. The GRS 1915+105 is the only black hole binary that reaches near Eddington luminosity consistently, making it the only likely candidate for radiation pressure instability.

However, in black hole systems like Cygnus X-1, the outer accretion disc behaves mostly as expected from classical models, such as the Shakura–Sunyaev disc, especially when describing long-term brightness changes in these systems. The reason is that most of them can be explained by the Hydrogen ionization instability model, which does explain their variability over time, but their observed X-ray spectra are far more complex In black hole systems like Cygnus X-1, the outer accretion disc behaves mostly as expected from classic models like the Shakura–Sunyaev disc, especially when explaining long-term changes in brightness. This is supported by the fact that many of these systems follow the hydrogen ionization instability model, which helps describe their variability over time. However, these standard disc models do not fully explain the observed X-ray spectra, which are far more complex.

1.2 Hard state, Soft states and Transition state

Radiations produced by the accretion disk can be a result of different types of emission[29],such as emission from the disk, emission from the hot electrons in the Corona, and synchrotron. or jet emission. The combination of these processes determines the shape of the X-ray spectrum observed.

In a soft state, also known as the High State/Thermal-dominant State, most radiation results from thermal emission, and the spectrum lies in the soft X-ray range (below 10 keV). This thermal emission most likely comes from a hot, optically thick accretion disc. However, the spectrum also has a high-energy tail (up to hundreds of keV), which can´t be explained by the standard disc model. In a hard state, also known as a low state, the spectrum has a much higher energy component (around 100 keV). This suggests that most of this energy originates from optically thin regions of the disk, most likely the corona, which produces a suitable environment for energy to remain high. Black hole X-ray binaries (BHXRs) alternate between these two states. These transitions could be related to a change in the accretion disk, a change in the structure of the corona, or could be associated with changes in the disk truncation radius (radius at which the accretion disk no longer behaves like a standard optically thick, geometrically thin accretion disk).

At first, Soft states and Hard states were named High and low states based on X-ray count rate observed in the energy range 2-10 keV, but after covering a broader energy range, observation showed us that the bolometric luminosity doesn´t change as dramatically as it was thought previously, which led researchers to change their names based on their spectral state.

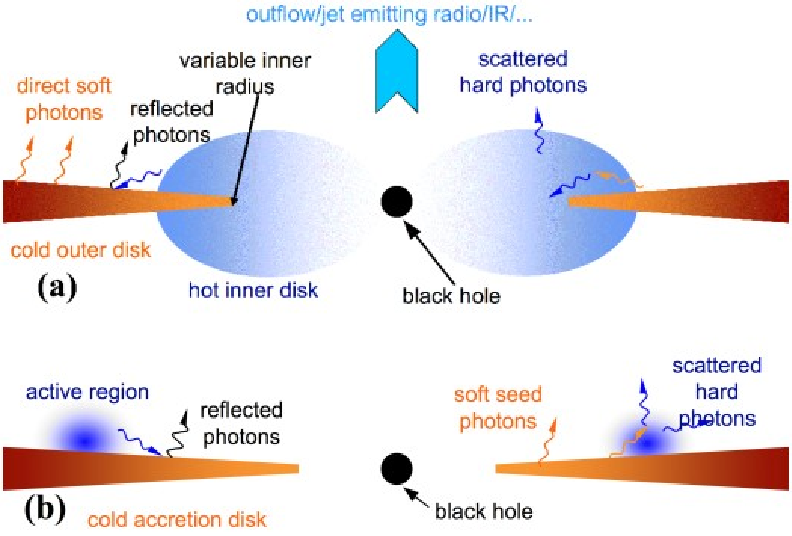

Figure 3: (a) In the hard state, the setup likely looks like this: There is a hot inner region of the accretion flow close to the black hole, and around it is a thicker, cooler accretion disk. This hot inner area is also the base of the jet (the part of the jet going in the opposite direction is left out to keep things simple). The cooler disk doesn't go all the way to the center—it stops some distance out—but it still overlaps with the hot inner region. The cooler disk gives off soft (low-energy) photons, which get scattered to higher energies by the hot inner flow (this is Compton upscattering). Also, some of the high-energy light from the hot flow bounces off the disk, which is known as Compton reflection. (b) In the soft state, things are a bit different: Now, the cool accretion disk extends much closer to the black hole , reaching nearly to the innermost stable orbit. Above this disk, there are flaring or active regions (areas where energy is released suddenly). Soft photons from the disk are scattered to higher energies by these flares, and some of the radiation from the flares is also reflected off the disk[8].

Cygnus X-1 also transitions between hard and soft X-rays, as visible from Figure 4. Although it occasionally transitions into the soft state, it stays mostly in the hard state. Spectra in the hard state are mostly dominated by a power law, with a photon index of 1.6-1.8 and a high-energy cut-off at 100 keV, along with a Compton reflection signature that includes the Fe Kα line. At energies lower than ~ 3 keV, the soft state appears as a blackbody-like component.[11]

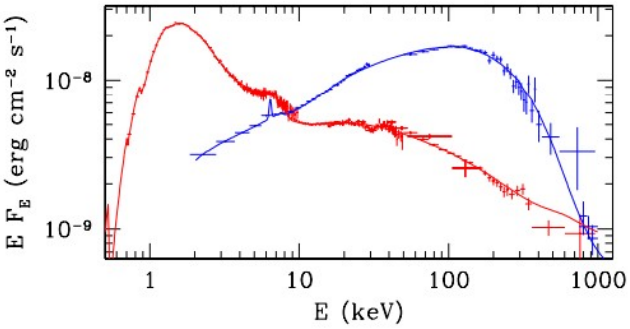

Figure 4: The spectral states of Cyg X-1 are shown by soft (red color) and hard (blue color) states. [11].

The accretion disk primarily emits thermal soft X-ray, but those photons enter the corona, and they go through repeated Compton inverse scattering, which explains the high-energy tail observed in this spectrum of Cygnus X-1 in Figure 4.

Another possible explanation for the low-hard state is that, at low mass accretion rates, the density of the inner accretion flow drops, resulting in fewer particles for collisions. Consequently, the inner flow becomes optically thin. Protons are more massive than electrons, so they gain more gravitational energy, making them hotter, while electrons are comparatively cooler because they radiate efficiently, resulting in a two-temperature plasma. Protons don't radiate efficiently, so, as a result, pressure increases, the inner disk puffs up, and the disk becomes geometrically thick; radiation occurs via non-thermal processes such as Compton scattering, bremsstrahlung, and synchrotron emission.

This type of hot, optically thin inner flow is described by the ADAF model[20], also known as the inward energy flow model, where most of the energy produced by friction is carried inward towards the black hole by advection instead of being radiated away, so in this case, advection is the main cooling process. The LHAF model[28], also known as the Luminance hot accretion flow model, has a denser accretion disk. When this dense matter falls inward, compressional heating heats the gas, showing that under these conditions, advection can also act as a heating process [19] [28]. Additionally, MRI also plays an important role in influencing these flows and can explain the physics behind jet formation.

According to the early model by Shapiro, Lightman, and Eardley (SLE76), protons that are heated by gravitational energy pass this energy to electrons through Coulomb Collisions [24]. Since electrons are efficient radiators, they emit this energy through bremsstrahlung and Compton scattering, but even a slight increase in temperature, in this case, can cause a problem. As protons become hotter, Coulomb coupling becomes less efficient, reducing the rate at which Energy is transferred from the protons to the electrons. Protons began to lose energy less efficiently, thereby increasing the temperature, triggering a positive feedback loop, and rendering the flow thermally unstable.

On the contrary, accretion flows that include advection are much more stable because in these flows, ions lose energy not only by transferring their energy to electrons but also by carrying the matter inward with the flow. In this case, an increase in temperature also makes cooling through advection more efficient, helping the system remain stable. This flow model aligns well with predictions from models that include magnetic field and turbulence simulations, such as those studying MRI, and suggests that advection, together with the magnetic field, helps maintain the flow's stability.

State transitions in low-mass X-ray binaries (LMXBs) are more complex than in systems such as Cygnus X-1. While Cygnus X-1 shows transitions between hard and soft states within a narrow range of luminosities, in LMXBs these transitions occur over a wide range of luminosities (Same can be seen from a comparison of the spectra of Cygnus X-1 and GX 339–4, shown in Figure 5, Cygnus X-1 undergoes state transitions within a narrow luminosity range, while GX 339–4 experiences transitions over a much wider range of luminosities, making its spectral changes more dramatic). This behavior is linked to unsteady mass transfer onto the compact object in LMXBs; matter piles up in the outer accretion disk due to disk instability and falls toward the inner disk during outbursts. During an outburst, the accretion rate and density increase, allowing efficient cooling and the formation of an optically thick disk. A geometrically thin, optically thick disk is associated with the soft state. As the outburst decays due to reduced mass transfer from the companion, the accretion rate decreases, and the inner disk recedes, resulting in lower density and insufficient cooling. The flow becomes hot and optically thin, producing the hard state. Because the disk structure depends on its prior state, the hard-to-soft and soft-to-hard transitions occur at different luminosities, leading to hysteresis in the light curve. This difference is very obvious in GX 339-4 because of strong outbursts and larger changes in accretion rate [8].

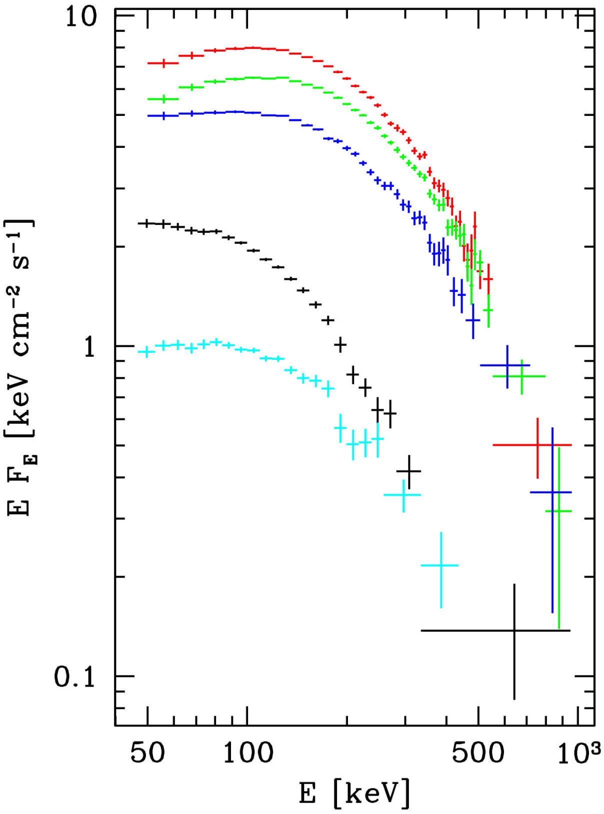

Figure 5: Displays the hard-state OSSE spectra for Cyg X-1 and GX 339–4. The top three spectra (colored red, green, and blue) correspond to Cyg X-1, with data averaged from 1991 to 1996 observations. These spectra are categorized based on the 100 keV flux. The two spectra at the bottom (in black and cyan) represent GX 339–4, derived from observations conducted in 1991 and 1997 [8].

Very High State, known as Steep power-law state, was also initially thought to be a very bright state. However, over time, researchers realized that it doesn´t always occur at the brightest times. Instead, it is actually related to the transition between soft state and hard state because the brightness of the system mainly depends on the accretion disk and the prior history of a system. That´s why its spectrum is mostly dominated by the soft state spectrum with a very steep power tail extending to higher energies. This shows that this state is somewhere in between the two states. Ultrasoft spectra, observed in systems like GX 339-4 and GRS 1915+105, shown in Figure 6, are sometimes observed at even higher luminosities than the Steep power-law state. This shows that the system can reach higher luminosities while it's still in a similar spectral state. During ultrasoft states, the system can continue to get brighter without switching back to a hard state, indicating that the transition between states is not always instantaneous and depends on evolution and prior history of the accretion disk.

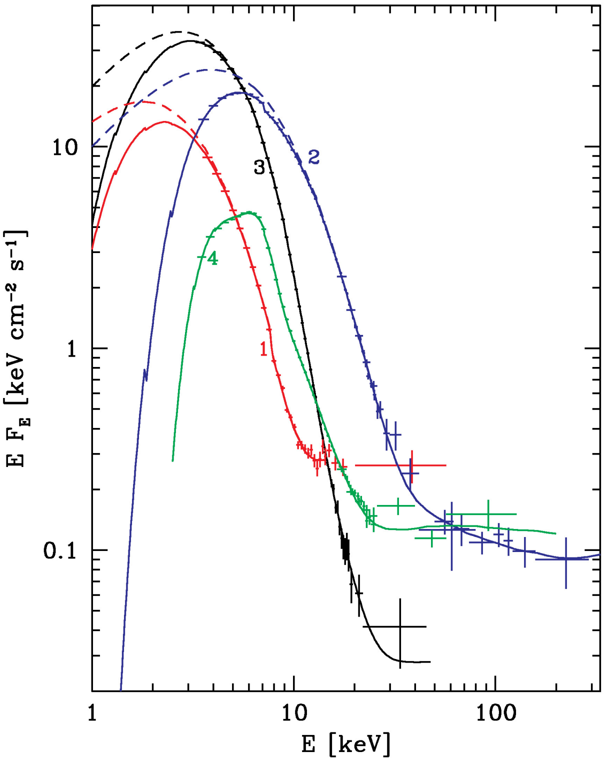

Figure 6: Ultrasoft spectra from black hole binaries are shown in the figure. Spectrum 1 represents the brightest state of GX 339–4 observed by RXTE. Spectrum 2 corresponds to one of the brightest states of GRS 1915+105. Spectrum 3 is taken from XTE J1550–564, while spectrum 4 shows the average ultrasoft spectrum of Cyg X-3[8]

Furthermore, the high tail in ultrasoft spectra shows $\Gamma = 2$, which is harder than in the case of the Steep power-law state, where $\Gamma = 1.6$ to 1.8, though we don't have any explanation for it yet.

In black hole binaries, the X-ray spectrum changes because the corona reacts to how many soft photons it receives from the accretion disk. When more soft photons enter the corona, they cool the electrons more efficiently through inverse Compton scattering, which changes the shape of the X-ray spectrum. This is the standard and widely accepted explanation. An alternative idea is that the X-rays come mainly from synchrotron radiation produced by non-thermal electrons that follow a power-law energy distribution. However, this explanation has problems. Small changes in the number or energy of these electrons would produce large spectral changes that are not seen in observations. In addition, if synchrotron radiation were the main source of X-rays, whenever X-rays change, the radio and infrared bands should show even bigger changes, but models predict much weaker variability in the radio and infrared bands than what is actually observed, which makes this explanation less likely.

In sources like GX 339–4, observations show a strong correlation between radio and X-ray flux over certain energy bands. This suggests that the corona supplies energetic particles that help launch the jet, while also producing X-rays. However, this correlation does not mean that the radio and X-rays are produced by the same radiation mechanism. The radio emission is dominated by synchrotron radiation in the jet, whereas the X-rays are produced mainly by Comptonization in the hot flow.

AGNs, which can be thought of as larger-scale versions of black hole X-ray binaries, also show a correlation between infrared and X-ray emission. First, it was thought that both emissions come from synchrotron or synchrotron self-Compton emission. However, later observations of Seyfert galaxies (AGN) showed a clear high-energy cutoff in their X-ray spectra, very similar to what is seen in sources like Cygnus X-1. Such a cutoff is naturally explained by thermal Comptonization and is difficult to reproduce with pure synchrotron models. This suggests that the X-rays are mainly produced by the corona, while the infrared emission is linked more indirectly to the overall accretion process. So, even though they are linked, they are not produced by the same process. Additional support for a compact X-ray-emitting region came from the fact that variability in Cygnus X-1 drops rapidly above about 100 Hz, indicating that the fastest variations are limited by the size and physical conditions of the inner accretion flow close to the black hole.

Recent observations with RXTE, including the PCA and HEXTE instruments, have revealed extremely fast and intense flares in black hole binaries like Cyg X-1. These flares occur on millisecond timescales and can reach peak brightness more than ten times the normal emission. During the strongest flare observed, the HEXTE detectors recorded the event clearly (as seen in figure 7), confirming that it originated from Cyg X-1 [8]. This observation supports the idea that such flares come from the innermost regions of the accretion disk, because only matter very close to the black hole can vary on such short timescales. For example, in the extended soft state of 2002, one flare reached a luminosity about 30 times the persistent level, rising in just 2 milliseconds. This corresponds roughly to the light-crossing time of the inner disk around a 10 solar mass black hole and is about half the orbital period at the innermost stable orbit. The most powerful flares reach roughly 0.3 times the Eddington luminosity, showing that these are extreme, rapid events.

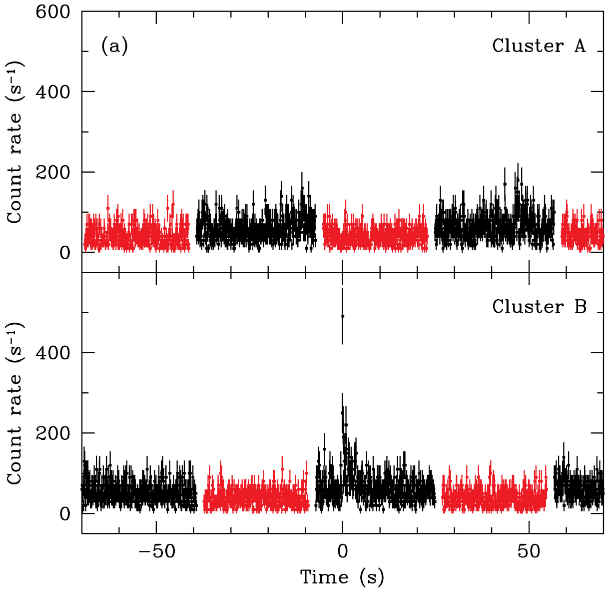

Figure 7: Presents the count rates recorded by two HEXTE units during the strongest observed flare. These units alternate between observing the source (Cyg X-1, shown in black) and the background (in red), located about 1° away. The flare's location aligns with the direction of Cyg X-1 to within an accuracy of less than 1° [8].

Similar millisecond flares have also been seen in other systems such as XTE J1118+480 and GX 339-4, suggesting that such events may be common in black hole binaries, though more data are needed to confirm this. The exact cause of these flares is still debated, but their extremely short timescales point to the innermost disk region. Possible explanations include rapid magnetic field amplification, sudden changes in the accretion flow state, or fast release of energy above the disk surface.

1.3 Inner accretion flow

The inner accretion flow structure is crucial for understanding the observed radiation. Recent studies tend to focus significantly on the innermost regions of the accretion disk. The innermost regions of the accretion disk have strong gravitational effects, which seriously affect the emitted radiation. With techniques like X-ray spectroscopy and timing techniques, the geometry of the inner disk can be inferred, and the sources of X-ray emission can be identified. Another powerful technique is polarimetry. Polarimetry measures the direction and degree of polarization of emitted X-rays, which can provide us with information about the inner disk, like the disk orientation, the corona´s structure, and the effects of relativistic light bending.

The innermost stable circular orbit (ISCO) sets the inner edge of the disk. Near this edge, relativistic effects, including frame dragging around a spinning black hole, strongly influence how the plasma moves and behaves. Studies show the direction of X-ray polarization is aligned within about 5 degrees of the radio jet axis, suggesting the idea that the jet launching is related to the inner accretion flow. Noble, Krolik, and Hawley (2010) [21] studied how magnetic stresses in the innermost parts of an accretion disk around Schwarzschild black holes depend on physical parameters, particularly the disk thickness (H/R) and magnetic field geometry. Traditional thin-disk models assume that the torque at the ISCO is effectively zero, meaning the stress there is negligible. This simplifies the calculation of black hole spin and disk emission by assuming that the inner disk does not transfer torque to the outer disk. However, simulations that include magneto-rotating instability (MRI) show that magnetic stresses can continue through and inside the ISCO, affecting how the inner accretion flow behaves and how energy is dissipated

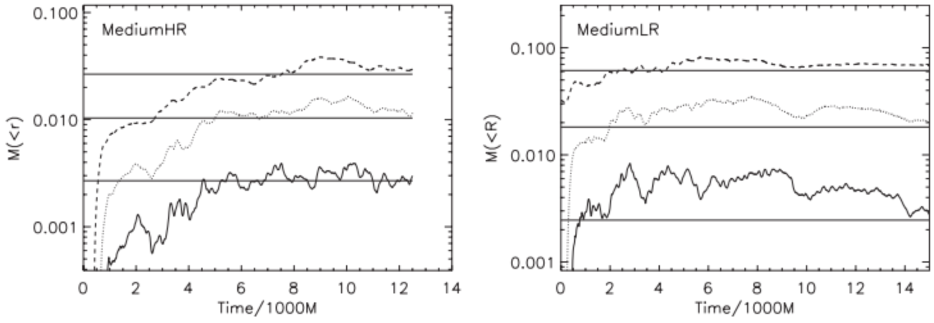

Figure 8: Depicts magnetic stress distributions near the ISCO and plunging region, showing dependence on disk thickness; Figure compares accreted angular momentum profiles for different magnetic field topologies, highlighting the role of magnetic geometry[21].

Figures 8 and 9 show that magnetic stresses in the inner disk decrease as the disk becomes thinner. Thin disks approach the classical zero-stress condition at the ISCO, while thicker disks show stronger stresses inside the ISCO. The shape, orientation, and structure of the magnetic field also strongly impact the stress levels; for example, different initial field geometries yield different stress levels. These stresses influence the angular momentum transferred to the black hole and can alter the disk's radiative efficiency, thereby affecting the amount of energy emitted as radiation.

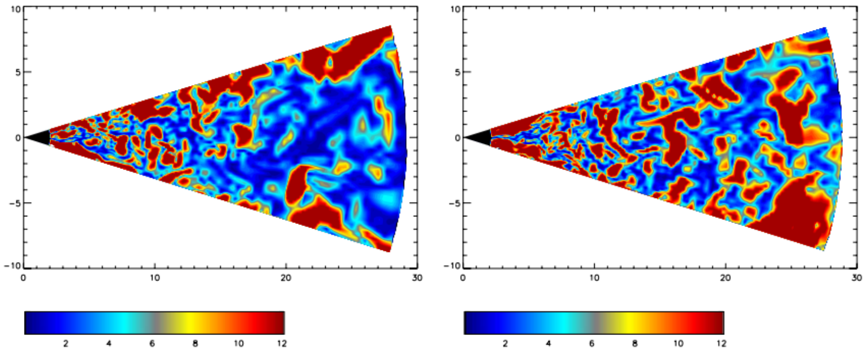

Figure 9: Figure displays radial profiles of angular momentum flux, revealing continued stress inside the ISCO for thicker disks and a sharper drop for thinner disks[21].

Understanding the behavior of stresses near the ISCO is therefore crucial for accurate modeling of black hole spin and disk emission. In this thesis, magnetic field effects have been neglected to simplify the model; however, they could be included in future work to improve its realism.

1.4 Cygnus X-1

Cygnus X-1 is one of the most well-known X-ray binary systems in astrophysics. It lies in the constellation Cygnus, approximately 2.22 kiloparsecs (7,250 light-years) from Earth. It consists of a supergiant star orbiting a stellar-mass black hole, which is the source of the X-ray emission we observe. This stellar-mass black hole is 21.2 times heavier than the sun, while the companion star is 40.6 times heavier than the sun. The companion star is extremely hot and luminous. It is an O-type star and orbits around a black hole in an elliptical orbit with a period of about 5.6 days. However, because the star is so hot, stellar winds are also blowing off the star, and the star nearly fills its Roche lobe because it is very large and orbits close to the black hole, so this wind is caught by the strong gravitational pull from the black hole so, in this case, accretion can be wind fed and unlike low mass X-ray binaries, doesn‘t purely come from Roche lobe flow. That's why fluctuations in wind can change the accretion rate and X-ray emission.

One of the most interesting things about this system is that its black hole has a 0.98 spinning parameter. A black hole´s spinning parameter is dimensionless and is used to measure the spin of a black hole. 0 represents a non-spinning black hole, and one refers to a spinning black hole. Hence, 0.98 shows that Cygnus X-1 is rotating extremely fast.

In an X-ray binary system like Cygnus X-1, hot material that is pulled by such a fast-spinning black hole gets heated to a really high temperature due to viscous dissipation and strong gravitational forces, and emits X-rays as it moves inward, which are visible during observation.

Cygnus X-1 is classified as a microquasar, a term used for stellar-mass black holes that launch relativistic jets. These jets launch nearly perpendicular to the axis of the accretion disk and move at a speed closer to light. These jets in Cygnus X-1 are observed in radio wavelengths, and their origin is believed to be near the inner accretion disk.

Cygnus X-1 is known for switching between different X-ray spectral states. Soft X-rays mostly come from thermal radiation coming from the inner accretion disk. Hard X-rays come from the hot ionized corona above the accretion disk; this state is the most variable state. The intermediate state is between the soft and hard states; it has both thermal and non-thermal emissions. This state is associated with either changes in the accretion disk's flow and geometry or in the corona's behavior. This state has a timescale of days to weeks.

The IXPE (Imaging X-ray Polarimetry Explorer) satellite, from polarimetric observations of Cygnus X-1, found that X-rays from Cygnus X-1 are polarized. The degree of polarization is approximately 4 degrees, which is relatively low but still detectable. The polarization direction is aligned with the jet axis. This suggests that there´s a connection between the X-ray emission and jets. Several models have been developed to study the properties and behavior of X-ray emission in Cygnus X-1. These studies provide valuable insights into the fundamental processes occurring around black holes, particularly accretion, X-ray emission, and jet formation.

1.5 X-ray polarimetry

X-rays are emitted from many distinct parts of a black hole. The accretion disk emits a thermal spectrum (mostly soft X-rays), while the corona emits a power-law spectrum (mostly hard X-rays). X-rays from the corona that are reflected off the disk produce fluorescent lines and a Compton hump. Jets or winds can also contribute to the spectrum. The relative proportion of these components changes depending on the spectral state of the black hole and the amount of gas or dust along the line of sight. General relativity also plays an important role in shaping the observed spectrum. The black hole's gravity bends the paths of photons, altering the apparent brightness and geometry of the emission. Gravitational redshift (from general relativity) and Doppler effects (from special relativity) shift the photon energies, distorting the observed spectrum. While determining how much each component contributes, different combinations of physical parameters of black holes (such as disk tilt, black hole spin, or corona size) can produce very similar spectra. For example, a disk that is slightly more tilted around a black hole with slightly lower spin may produce a spectrum nearly identical to that from a disk with less tilt but higher spin. Because the spectrum is just a plot of intensity versus energy, many parameter changes can compensate for each other and leave the overall shape almost unchanged. Hence, it is not possible to determine all physical properties of black holes using spectroscopy alone. So, we need polarimetry. Polarimetry measures the direction and degree of polarization of X-rays. The accretion disk and corona produce X-rays with specific polarization signatures that depend on geometry, inclination, and relativistic effects. For example, light bending and scattering change the polarization angle and degree in ways that spectroscopy cannot capture. By adding polarization data to the spectral information, the allowed physical models can be narrowed, resolving degeneracies. For example, it becomes possible to distinguish between a disk seen edge-on versus face-on, leading to more robust measurements of black hole spin and the physics of the accretion flow. Relativistic effects are particularly prominent near the photon orbit, $r_{\rm ph} = \frac{3GM}{c^2} = 4.43\,\frac{M}{M_\odot}$ km for a non-rotating black hole[9]. Around 6–7 keV, iron atoms in the disk emit a strong X-ray line. This iron line is usually unpolarized because it is produced by fluorescence (re-emission of photons), which doesn't strongly align the light waves.

The emission angle, incident angle, and relative azimuthal angle are not the same across the accretion disk because of the relativistic effects and thus affect the local polarization vector significantly across the disk. The transfer function acts as a weight, where in some parts of the region it increases emission, while in other parts it decreases outgoing radiation.

The transfer function modifies how different disk regions contribute to the observed flux and polarization. Here, G is the transfer function.[9, 10]

$$I_0 = I_{\mathrm{refl}} + I_{\mathrm{prim}} = \int_{\Sigma} \mathrm{d}S\, G \left(I_{\mathrm{disk}}^{\mathrm{cont}} + I_{\mathrm{disk}}^{\mathrm{line}} \right) + I_{\mathrm{prim}} \tag{3}$$

$$Q_{\mathrm{o}} = \int_{\Sigma} \mathrm{d}S\, G\, P_{\mathrm{disk}}\, I_{\mathrm{disk}}^{\mathrm{cont}} \cos \left[2 \left(\chi_{\mathrm{disk}} + \psi \right) \right] \tag{4}$$

$$U_{\mathrm{o}} = \int_{\Sigma} \mathrm{d}S\, G\, P_{\mathrm{disk}}\, I_{\mathrm{disk}}^{\mathrm{cont}} \sin \left[2 \left(\chi_{\mathrm{disk}} + \psi \right) \right] \tag{5}$$

Relativistic effects break the symmetry of the disk emission pattern. This leads to non-axisymmetric weighting of the polarization contributions because of the non-axisymmetry; the observed polarization angles are not parallel or perpendicular; in fact, they can vary continuously, depending on the observer's inclination, black hole spin, and emission geometry. Local intensities, in these equations, also act as weights due to the energy shift, which can move the unpolarized iron line, the iron edge, and the Compton hump features in or out of the energy range we are looking at.

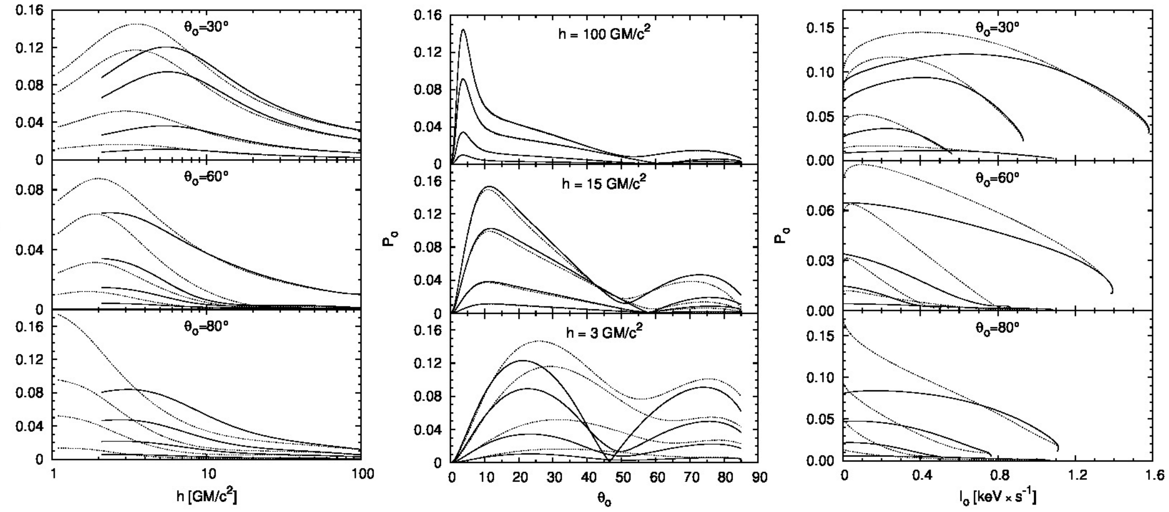

Figure 10: Graphs on left show dependance of polarization angle at infinity on height (solid lines are for non rotating blackholes and dotted lines are for kerr metric), the graph in the center is showing dependance on inclination at infinity and graph on right is showing depandance on total intensity at infinity, while photons energy ranges are 2–6, 6–10, 10–20, and 20–50 keV[9].

As visible from Figure 10, at low inclinations, light from different parts of the disk is nearly symmetric around the observer's line of sight. This symmetry causes the electric vectors of scattered photons to cancel each other out, reducing the net polarization. In other words, reflection still occurs, but the geometry makes the combined polarization weaker. At high inclinations, relativistic effects (Doppler boosting, gravitational redshift) shift the iron edge (the sharp drop in reflection spectrum above the iron line). This energy shift changes where the strongest reflection occurs, leading to more anisotropic scattering. The stronger asymmetry allows the reflected photons to add coherently to produce a higher net polarization enough to counteract the normal tendency of high inclinations to reduce polarization. The primary corona emits more low-energy photons than high-energy ones. As energy increases, the direct (unpolarized) primary emission drops off faster than the reflected emission. Above 20 keV, the reflected component (the Compton hump) dominates. Reflection involves Compton scattering, which naturally produces stronger polarization than the primary emission[18]. Therefore, the net polarization fraction is highest in the 20–50 keV range, making this band ideal for X-ray polarimeters.

In order to understand the dependence of the relativistic rotation of the polarization angle on observer inclination, we need to consider a critical point (a point where photons are emitted perpendicular to the accretion disk), so we can take into account the effects of special relativistic aberration. For small inclination, the observer is nearly above the disk. A photon emitted at a very low orbital speed will easily be able to reach the observer. In this case, the critical point is also far away from the center of the black hole. For large inclination, the photon has to move at a high orbital speed in order to reach the observer because now the observer is near the edge of disk and critical point will be near the black hole center, as the role of the general relativistic aberration and light bending becomes notable and as a result the location of the critical point is behind the black hole. In the Inner disk (radii below the critical radius), orbital speed is high, and gravity is strong, so relativistic effects are strong. Polarization angle can rotate through the full range (−180° to +180°). While in an outer disk (radii above the critical radius), orbital speed is slower, and gravity is also weaker. Thus, relativistic effects become weaker. Polarization angle rotates only a little, and the farther out you go, the narrower the range of rotation. High-spinning black holes also have a high degree of polarization.

Thermal radiation is produced mainly from Thomson scattering in the disk atmosphere[2]. Because the local polarization is always in the same simple directions (parallel/perpendicular),relativistic rotation as the photons travel to the observer twists these vectors differently for different parts of the inner disk. This creates cancellation, reducing the net polarization(depolarization).In contrast, in the reflection process, the local polarization varies with scattering geometry, so after relativistic rotation, the vectors can add more coherently and have higher net polarization. When the corona is close to the black hole, the inner disk is strongly illuminated. Inner disk dominates the reflection and has high net polarization (because inner-disk reflection is less depolarized). If the lamp is higher, light spreads over the outer disk and the inner disk contributes less, which results in lower polarization. Different parts of the disk emit different local polarization. When a photon travels from the co-moving frame of the local disk material to the observer, the orientation of the polarization vector is changed. The orientation depends on which part of the disk photons have been emitted from. The overall net polarization depends on the weight of the transfer function and local intensity (proportional to the incident intensity from the primary source). That´s why the corona height will determine the radii at which light will be most illuminated and thus can change the local polarization degree and angle[6, 25, 12].

For thermal radiation, Local polarization is always either parallel or perpendicular to the disk plane. Thermal emission where all local vectors are aligned (parallel/perpendicular). When adding up all the contributions from the disk, due to relativistic

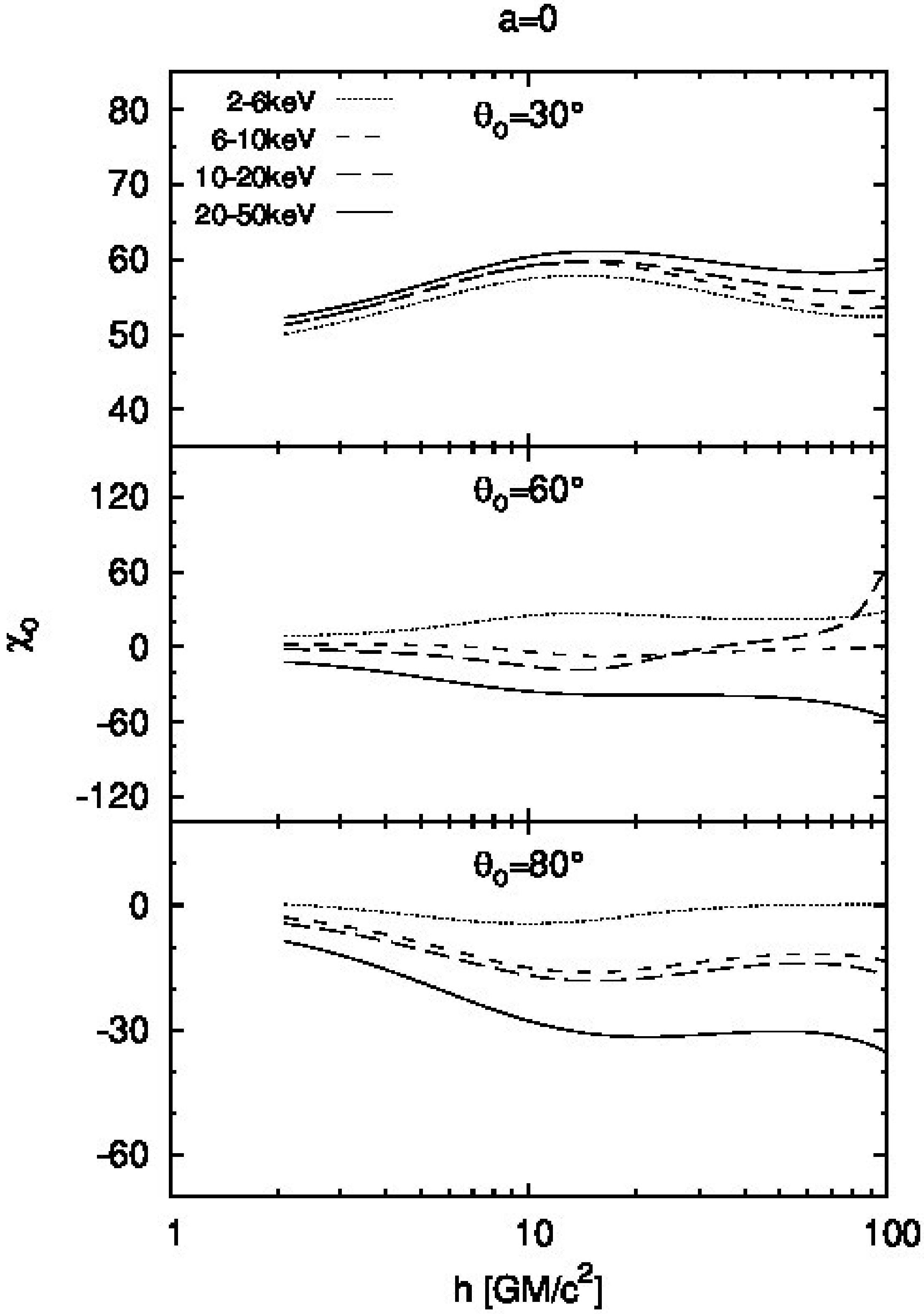

Figure 11: Shows the dependence of polarization angle at infinity on height. Solid lines are for non-rotating black holes, and dotted lines are for the Kerr metric. Photons' energy ranges are 2–6, 6–10, 10–20, and 20–50 keV[9].

rotation, the rotated vectors partially cancel, and the net polarization is decreased. while for reflected radiation, the local polarization angle depends on scattering geometry. Due to the combination of local scattering angle and relativistic rotation, the next local polarization is much less.

Also, The Kerr black hole is more polarized compared to the Schwarzschild case. However, at 30 and 80 degrees, the Schwarzschild BH is more polarized. In the Kerr case, the polarization degree changes with corona height in a way that mirrors the ratio of reflected to primary light (Irefl/Iprim).In the Schwarzschild case, even when reflected light is weak, polarization can still be really strong due to the missing inner disk. At large heights (h is nearly or equal to 30GM/c2), the polarization degree and polarization angle don´t change. At low inclinations (almost face-on), the inner region (below the critical radius) dominates.

Net polarization increases, As inclination grows, more emission from above the critical radius contributes. The two regions start to cancel and result in a drop in polarization. At higher inclinations, the outer disk dominates. Polarization rises again, but with the opposite orientation. However, at very high inclinations, Reflection becomes faint (grazing view), so the polarization degree drops again. The polarization angle at infinity is more sensitive and more complex. Small changes in height or angle can noticeably change the polarization direction at infinity. At infinity, the inner region below the critical radius contributes to net polarization even at high inclinations. Although at a high inclination, only the outer region contributes to determining the polarization.

1.6 X-ray polarimetry in Cygnus X-1

Cygnus X-1, while switching between different spectral states, shows variability in its X-ray emission. The first polarization observation of Cygnus X-1 was done with OSO-8 and measured a polarization degree of $2.44 \pm 1.07\%$, and a polarization angle of $-18° \pm 13°$ at 2.6 keV, with the measurement taken from north to east on the sky [17]. The International Gamma-Ray Astrophysics Laboratory (INTEGRAL) found a very high polarization degree of 65% and a polarization angle of 224° in the 0.4–2 MeV range [16, 13]. AstroSat measured a polarization degree of 23% and a polarization angle of 236° in the energy range of 100–380 keV in the hard–intermediate state [3]. PoGO+ observations by Chauvin et al. [4, 5] measured a polarization degree of less than 8.6% with 90% confidence, and the polarization angle in the 19–181 keV range was found to be aligned with the jet axis. In the 2–8 keV energy range, the Imaging X-ray Polarimetry Explorer (IXPE) observed that the polarization degree in Cygnus X-1 is about $4.0 \pm 0.2\%$, and the polarization angle was found to be $-20.7° \pm 1.4°$ in the hard state [15, 26].

The lamp-post corona model and the extended corona model are the two competing models for describing corona in BHBs, as shown in Figure 12. In the lamp/post model, corona size is small, corona is located above the inner accretion disk, close to the event horizon and is strongly influenced by GR/SR while extended corona model have larger corona and the inner disk evaporates or puffs up into a hot, geometrically thick corona, so, primary coronal emission comes from an extended region, and the influence of GR/SR is small.

PoGO+ observations by Chauvin et al. [4, 5] measured that most of the X-ray emission observed during the hard state originates from regions where relativistic effects are weak. This supports the idea of an extended corona model. Previous spectral/timing analyses proposed this model. This model provides a plausible explanation for the transition

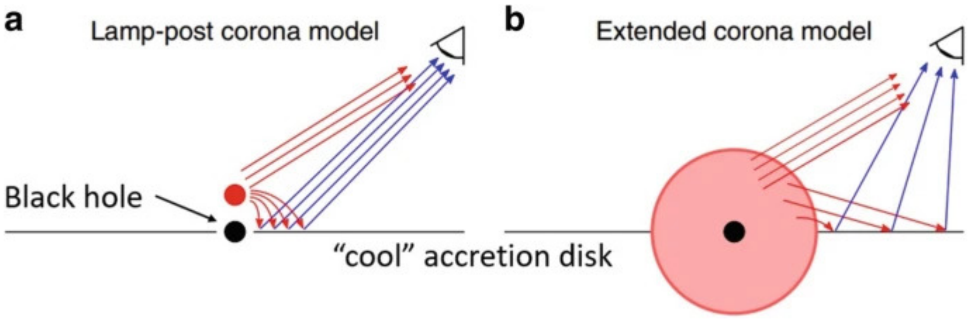

H

Figure 12: (a) shows lamp-post corona model, the red lines represent photons coming from corona, while blue shows photons coming from accretion disk (b) shows extended corona model where corona is extended in the inner region of accretion diskChauvin et al. [4] .

between the hard and soft states in Cygnus X-1. This model suggests that the shrinkage of the extended corona and the inward extension of the truncated disk to the ISCO are consistent with this transition.

This extended corona is explained by two further possible models: the sandwich disk model and the truncated-disk model. The sandwich disk model predicts a cold, optically thick disk extending to the ISCO, and a hot plasma layer above and below the disk. The truncated-disk model, on the other hand, predicts a thin outer disk that doesn´t extend to the inner region. Instead, it is replaced by a hot, geometrically thick, optically thin region in which photons scatter multiple times and escape, thereby creating strong polarization.

The sandwich disk model requires an inclination of nearly 65° to reproduce the observed polarization angle, while the truncated disk model can produce the observed polarization at an inclination of 45°, as shown in Figure 13. This is because, in the truncated disk, low-energy photon seeds must undergo multiple scatterings to reach the required X-ray energy. Both values are still higher than the observed binary inclination of approximately 27°, implying that the inner accretion flow is tilted relative to the binary orbital plane. Several theories have been proposed to explain this misalignment, including a supernova event in Cygnus X-1 and gravitational or frame-dragging effects, though other explanations also exist. X-ray polarimetry provides valuable insights into the geometry of the X-ray sources in Cygnus X-1. Polarization supports the idea that the accretion disk and jet launching region form part of a connected system. Observed polarization depends on Special and general relativistic effects. Relativistic aberration changes the observed polarization angle. The rapid motion of the disk material changes the apparent viewing angles of different regions, altering the polarization angle. Strong gravitational fields bend light due to general relativistic effects, which modify the observed polarization degree by changing the projected angles between the observer and the disk normal. Frame-dragging effects in Kerr spacetime introduce additional rotations to the polarization plane along the photon's trajectory, but here, we are ignoring frame dragging.

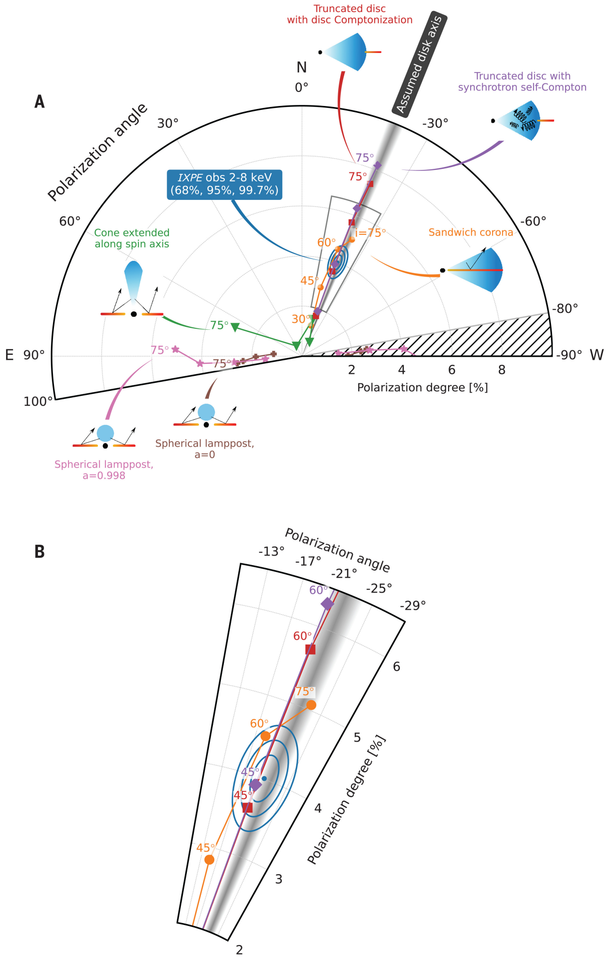

Figure 13: (a)The blue dot shows the measured polarization degree and angle, with blue ellipses indicating confidence levels (how sure we are about the measurement). The models assume the inner disk's spin axis points at about -22°, matching the radio jet's direction. The gray band shows the uncertainty in this direction. Different colored lines show predictions for various corona shapes and disk tilt angles. The small diagrams illustrate the black hole (black), corona (blue), and disk (orange-red) setups. Models where the corona extends along the disk fit the data better than those aligned with the spin axis.(b) shows zoomed measurements[14]

To account for these relativistic effects, the polarization of photons is tracked as they travel along curved paths in spacetime via parallel transport along null geodesics. Mathematical tools like the Walker-Penrose constants help simplify these calculations. Ray-tracing methods can then simulate how polarization appears to a distant observer, providing precise results, although they require significant computational effort.

Studies by Connors [6] and Dovciak [8] have helped us understand relativistic effects on observed polarization signatures in accretion disks, particularly in the Schwarzschild metric. However, in this paper, we present a faster analytical method that efficiently calculates relativistic effects on polarization, without the need for time-consuming ray tracing.

2 Methodology

In this paper, we adopted the analytical framework developed by Loktev [27] to examine how the polarization of emitted light depends on the observer's inclination. The Cartesian coordinate system has been used to describe the geometry of a flat disk surface. In the figure below, the disk normal $\hat{n}$ is along the z-axis, which is given as

$$\hat{n} = (0, 0, 1), \tag{6}$$

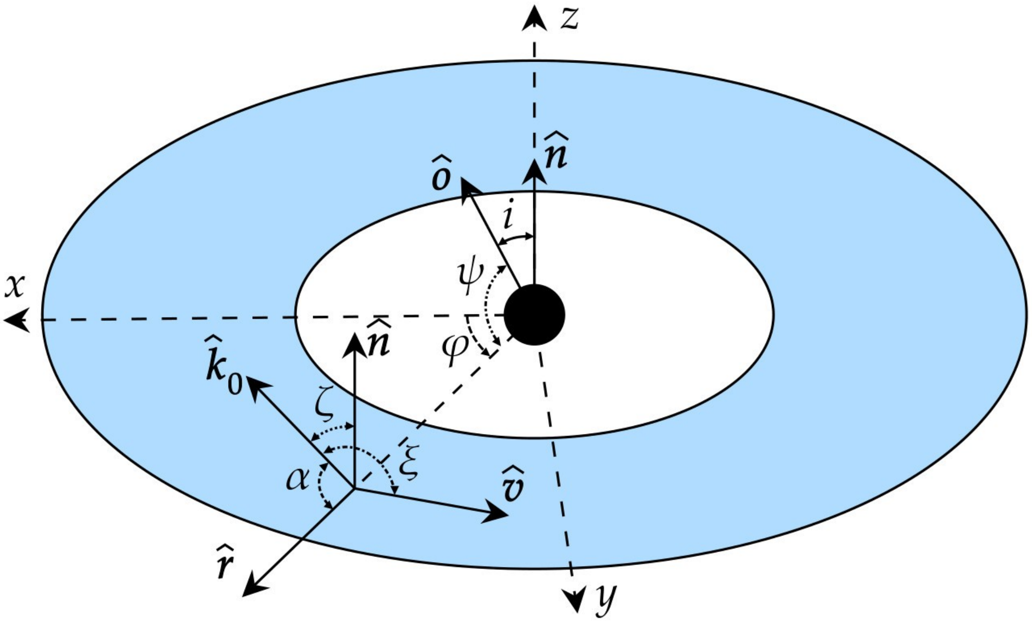

Figure 14: Geometry of non-rotating flat accretion disk. $\hat{v}$ here is the velocity of the photon and $\hat{r}$ is the radius vector, while $\hat{k}_0$ shows the photon momentum, which makes an angle with the disk normal. It also makes an angle with velocity, and vector $\hat{o}$ here is pointing in the direction of the observer and makes an angle i with the disk normal, while φ is the azimuth angle measured from the x-axis.

and the x-axis is along the projection of the line of sight. $\hat{o}$ is the observer's line of sight, which lies in the x-z coordinate and hence has been defined as

$$\hat{o} = (\sin i,\ 0,\ \cos i), \tag{7}$$

Here i is the angle of inclination from the disk normal to the line of sight. and $\hat{r}$ the radius vector of the surface element ds is in the xy axis and can be defined using the azimuth angle ϕ, which is the angle shown in the figure as from the x-axis to the radius vector.

$$\hat{r} = (\cos\varphi,\ \sin\varphi,\ 0) \tag{8}$$

The ψ is the angle the radius vector makes with the line of sight $\hat{o}$, hence

$$\cos\psi = \hat{r} \cdot \hat{o} = \sin i \cos\varphi \tag{9}$$

Photons move within one plane in the Schwarzschild black hole accretion disk. So, the direction of photon momentum is a linear combination of the observer vector $\hat{o}$ and the radius vector $\hat{r}$

$$\hat{k}_0 = A\hat{o} + B\hat{r} \tag{10}$$

By using the sine law, we can measure A and B and get the following value of $\hat{k}_0$

$$\hat{k}_0 = \frac{\sin\alpha\,\hat{o} + \sin(\psi - \alpha)\,\hat{r}}{\sin\psi} \tag{11}$$

Where α is the angle from the radius to the photon momentum

$$\cos\alpha = \hat{r} \cdot \hat{k}_0 \tag{12}$$

As apparent from the figure, the azimuthal vector and velocity vector are both parallel to each other. Hence, we can define the azimuth as

$$\hat{v} = \hat{\varphi} \equiv (-\sin\varphi,\, \cos\varphi,\, 0) \tag{13}$$

$\beta = \frac{v}{c}$ is the dimensionless velocity measured relative to the static observer at radius $r = R/R_s$, where R_s is the Schwarzschild radius given by the formula $R_s = \frac{2GM}{c^2}$

$$\beta = \sqrt{\frac{u}{2(1-u)}} \tag{14}$$

u here is gravitational compactness which has been defined as $u = 1/r$ and hence by putting the value of β we can define the Lorentz factor as

$$\gamma = \frac{1}{\sqrt{1-\beta^2}} = \sqrt{\frac{1-u}{1-3u/2}} \tag{15}$$

and Doppler Shift is

$$\delta = \frac{1}{\gamma(1 - \beta\,\hat{v}\cdot\hat{k}_0)} = \frac{1}{\gamma(1 - \beta\cos\xi)} \tag{16}$$

while ξ can be defined as

$$\cos\xi = \hat{v} \cdot \hat{k}_0 \tag{17}$$

Since $\hat{v}$ and $\hat{r}$ are both perpendicular to each other, only the first term of $\hat{k}_0$ remains. Hence

$$\cos\xi = \frac{\sin\alpha}{\sin\psi}\,\hat{v}\cdot\hat{o} = -\frac{\sin\alpha}{\sin\psi}\,\sin i\,\sin\varphi \tag{18}$$

And ζ can be defined as

$$\cos\zeta = \hat{n} \cdot \hat{k}_0 \tag{19}$$

Similarly, $\hat{r}$ and $\hat{n}$ are both perpendicular to each other, and thus, only one term of $\hat{k}_0$ remains here as well.

$$\cos\zeta = \frac{\sin\alpha}{\sin\psi}\,\hat{n}\cdot\hat{o} = \frac{\sin\alpha}{\sin\psi}\,\cos i \tag{20}$$

We boost to a frame S' moving with velocity $v\hat{v}$ relative to S. The Lorentz boost (with boost velocity v) acts on any 4-vector $A^{\mu} = (A^0, A)$ as

$$\begin{pmatrix} A'^0 \\ A' \end{pmatrix} = \begin{pmatrix} \gamma & -\gamma\beta^T \\ -\gamma\beta & I + (\gamma - 1)\,\hat{v}\hat{v}^T \end{pmatrix} \begin{pmatrix} A^0 \\ A \end{pmatrix}, \qquad \beta = \frac{v}{c}. \tag{21}$$

$$A'^0 = \gamma\left(A^0 - \beta \cdot A\right), \tag{22}$$

$$A' = A + (\gamma - 1)\,(\hat{v} \cdot A)\,\hat{v} - \gamma\,\beta\,A^0. \tag{23}$$

Apply the boost to $k^{\mu} = (\omega/c,\, k)$.
Using $A^0 = \omega/c$ and $A = k$, the transformed frequency is

$$\frac{\omega'}{c} = k'^0 = \gamma\left(\frac{\omega}{c} - \beta \cdot k\right) = \frac{\omega}{c}\,\gamma\left(1 - \beta\,\hat{v} \cdot \hat{k}_0\right). \tag{24}$$

In the primed frame,

$$k' = \frac{\omega'}{c}\,\hat{k}'_0 \tag{25}$$

Thus,

$$\hat{k}'_0 = \frac{k'}{\omega'/c} = \frac{\omega}{\omega'}\left[\hat{k}_0 + (\gamma - 1)(\hat{v} \cdot \hat{k}_0)\,\hat{v} - \gamma\beta\,\hat{v}\right]. \tag{26}$$

Then the Doppler factor will be given as

$$\frac{\omega}{\omega'} = \frac{1}{\gamma\left(1 - \beta\,\hat{v} \cdot \hat{k}_0\right)} \equiv \delta. \tag{27}$$

Therefore,

$$\hat{k}'_0 = \delta\left[\hat{k}_0 - \gamma\beta\,\hat{v} + (\gamma - 1)(\hat{v} \cdot \hat{k}_0)\,\hat{v}\right]. \tag{28}$$

ξ', ζ', α and ϕ' can also be derived

$$\cos\xi' = \hat{v} \cdot \hat{k}'_0 \tag{29}$$

because

$$\hat{k}'_0 = \delta\left[\hat{k}_0 - \gamma\beta\,\hat{v} + (\gamma - 1)(\hat{v} \cdot \hat{k}_0)\,\hat{v}\right]. \tag{30}$$

so,

$$\cos\xi' = \hat{v} \cdot \delta\left[\hat{k}_0 - \gamma\beta\,\hat{v} + (\gamma - 1)(\hat{v} \cdot \hat{k}_0)\,\hat{v}\right]. \tag{31}$$

Which reduces to

$$\cos\xi' = \delta\gamma\cos\xi - \beta \tag{32}$$

And similarly, we can get ζ' and α' angles in co-moving frame

$$\cos\zeta' = \delta\cos\zeta \tag{33}$$

and

$$\cos\alpha' = \hat{r}\cdot\hat{k}_0 \tag{34}$$

and ϕ' (azimuth angle in co-moving frame)can also be obtained by integrating $\cos\xi'$ and α' into the equations

$$\sin\phi' = \frac{\hat{k}_0'\cdot\hat{\varphi}}{\sin\zeta'} = \delta\,\gamma\,\frac{\cos\xi-\beta}{\sin\zeta'} \tag{35}$$

$$\cos\phi' = \frac{\hat{k}_0'\cdot\hat{r}}{\sin\zeta'} = \delta\frac{\cos\alpha}{\sin\zeta'} \tag{36}$$

2.1 Observed flux at fixed location

Specific flux coming from surface element ds at Energy E is

$$\mathrm{d}F_E = I_E\,\mathrm{d}\Omega \tag{37}$$

Where dΩ is the solid angle on the observer's sky corresponding to the surface element ds of the source. I_E is the specific intensity of radiation at infinity, and it is related to the corresponding intensity measured in the rest frame

$$\frac{I_E}{E^3} = \frac{I'_E}{E'^3} \tag{38}$$

$$I_E = \left(\frac{E}{E'}\right)^3 I'_{E'}(\zeta') \tag{39}$$

Here we use $I'(\theta)$ instead of $I'(r',\theta',\phi')$ because there is no variation in intensity when you rotate around the axis, and we are evaluating at a fixed radius. g is the total redshift factor that accounts for the relativistic Doppler effect δ and the gravitational effect $\sqrt{1-u}$

$$g \equiv \frac{E}{E'} = \delta\sqrt{1-u} = \frac{\sqrt{1-\frac{3u}{2}}}{1+\beta\sin i\sin\varphi\sin\alpha/\sin\psi} \tag{40}$$

The 2D surface element on this plane is made of radial and azimuthal increments:

$$dS = \sqrt{g_{RR}g_{\phi\phi}}\,dR\,d\phi \tag{41}$$

From the metric:

$$g_{RR} = \frac{1}{1-u}, \qquad g_{\phi\phi} = R^2 \tag{42}$$

thus

$$dS = \sqrt{\frac{1}{1-u}\cdot R^2}\,dR\,d\phi = \frac{R\,dR\,d\phi}{\sqrt{1-u}} \tag{43}$$

Surface element ds is given by

$$dS = \frac{R\,\mathrm{d}R\,d\phi}{\sqrt{1-u}} \tag{44}$$

and $\mathrm{d}s\cos\zeta'$ is the projection of this surface element onto the sky, so we can write the solid angle corresponding to this surface element as

$$\mathrm{d}\Omega = R\,\mathrm{d}R\,\frac{\mathrm{d}\varphi}{D^2\sqrt{1-u}}\mathcal{L}\cos\zeta = \frac{R_S^2}{D^2}\,\frac{r\,\mathrm{d}r\,\mathrm{d}\varphi}{\sqrt{1-u}}\,\mathcal{L}\cos\zeta \tag{45}$$

Where D is the distance from the source and $\mathcal{L}$ is the lensing factor[1, 22]

$$\mathcal{L} = \frac{1}{1-u}\,\frac{\mathrm{d}(\cos\alpha)}{\mathrm{d}(\cos\psi)} \tag{46}$$

We integrate the value of $\mathrm{d}\Omega$ into the specific flux equation and we get

$$\mathrm{d}F_E(r,\varphi) = g^3 I'_E(\zeta')\,\frac{\mathrm{d}S\cos\zeta}{D^2}\,\mathcal{L} \tag{47}$$

Now, by taking the integral of it, we get the total observed flux of the disk

$$F_E = \frac{R_S^2}{D^2}\int_{r_{\mathrm{in}}}^{r_{\mathrm{out}}}\frac{r\,\mathrm{d}r}{\sqrt{1-u}}\int_0^{2\pi}\mathrm{d}\varphi\,g^3\,\mathcal{L}\cos\zeta\,I'_{E'}(\zeta') \tag{48}$$

2.2 Stokes parameters

Since we have considered only linear polarization in this case (ψ and χ are not the same as defined before; I, p, ψ, and χ are just the spherical coordinates of the Cartesian coordinate), the ellipticity angle is

$$\chi = 0. \tag{49}$$

We substitute $\chi = 0$ into the Stokes definition

$$\cos 2\chi = \cos 0 = 1, \qquad \sin 2\chi = \sin 0 = 0. \tag{50}$$

Thus,

$$\begin{aligned} S_0 &= I, \\ S_1 &= Ip\cos 2\psi, \\ S_2 &= Ip\sin 2\psi, \\ S_3 &= 0. \end{aligned} \tag{51}$$

$$\boxed{\begin{pmatrix} S_0 \\ S_1 \\ S_2 \\ S_3 \end{pmatrix} = \begin{pmatrix} I \\ Ip\cos 2\psi \\ Ip\sin 2\psi \\ 0 \end{pmatrix}} \tag{52}$$

The direction of the polarization vector changes as it moves along the photon's trajectory due to gravitational light bending and aberration. However, the angle between polarization and the trajectory plane remains conserved, which helps us to derive simple formulas for the PA rotation angle. To compute polarization at the emission angle in the co-moving frame, we need a basis vector for the polarization vector. $\hat{n}$ and $\hat{k}$ both form two basis vectors

$$\hat{e}_1^0 = \frac{\hat{n} - (\hat{n}\cdot\hat{k}_0)\,\hat{k}_0}{\sqrt{1 - (\hat{n}\cdot\hat{k}_0)^2}} = \frac{\hat{n} - \cos\zeta\,\hat{k}_0}{\sin\zeta}. \tag{53}$$

$$\hat{e}_2^0 = \frac{\hat{k}_0 \times \hat{n}}{\|\hat{k}_0 \times \hat{n}\|} = \frac{\hat{k}_0 \times \hat{n}}{\sin\zeta}. \tag{54}$$

Thus, we can describe the specific intensity at (r, ϕ) in the direction ζ' which can be given by a Stokes vector as

$$\mathbf{I}_E(\zeta') = I_E(\zeta') \begin{bmatrix} 1 \\ p(\zeta')\cos 2\chi_0 \\ p(\zeta')\sin 2\chi_0 \end{bmatrix} \tag{55}$$

Where p is the linear PD of radiation, and it is invariant, meaning it does not change along the photon trajectory, while the polarization angle χ_0 is the angle between the polarization vector and the basis vector $\mathbf{e}_0^{\varphi}$, and we measure it in the counterclockwise direction.

$$\mathbf{M}(r, \varphi) = \begin{bmatrix} 1 & 0 & 0 \\ 0 & \cos 2\chi_{\text{tot}} & -\sin 2\chi_{\text{tot}} \\ 0 & \sin 2\chi_{\text{tot}} & \cos 2\chi_{\text{tot}} \end{bmatrix} \tag{56}$$

2.3 Total observed flux

We need the Mueller matrix for transforming the specific intensity vector, where χ_{tot} is the rotation angle of the polarization plane. Now we can add this Mueller matrix to the equation for the observed specific flux

$$d\mathbf{F}_E(r, \varphi) = g^3 \mathbf{M}(r, \varphi)\mathbf{I}_E(\zeta')\, dS \frac{\cos\zeta}{D^2} \tag{57}$$

and integrating it will give us the total flux.

2.4 Polarization angle

The angular distribution of radiation from the accretion disk only depends on the zenith angle ζ' and not on the azimuth φ' because of the axis symmetry of the disk. The polarization vector must be parallel to one of the bases and perpendicular to the other bases. We put $\chi_0 = 0$ or $\pi/2$ in the specific flux equation, transform it with the Mueller matrix, and integrate the results in the total flux, and then we can get the total observed Stokes vector.

$$d\mathbf{F}_E(r, \varphi) = g^3 I_E(r, \zeta') \begin{bmatrix} 1 \\ \pm p(\zeta')\cos 2\chi_{\text{tot}} \\ \pm p(\zeta')\sin 2\chi_{\text{tot}} \end{bmatrix} \frac{dS\cos\zeta}{D^2}\,\mathcal{L} \tag{58}$$

The total rotation of the polarization angle (PA) along the photon trajectory is

$$\chi = \chi_0 + \chi^{\rm tot} \tag{59}$$

The PA rotation can be computed directly from the rotation of the polarization plane and the projection of the polarization vector onto the sky, as viewed by the observer. The rotation by the general relativistic (GR) light bending effects is given by

$$\tan \chi^{\rm GR} = \frac{\cos i \, \sin \psi}{\tilde{a} \, \sin i + \cos \varphi} \tag{60}$$

where

$$\tilde{a} = \frac{1 - \cos\alpha \cos\psi}{\cos\alpha - \cos\psi}. \tag{61}$$

To account for relativistic effects, we need

$$\tan \chi^{\rm SR} = -\beta \, \frac{\cos\alpha \cos\zeta}{\sin^2\zeta - \beta\cos\xi}. \tag{62}$$

In a curved spacetime, photons do not reach the observer in a straight line. However, near the disk, photons propagate along $\hat{\mathbf{k}}_0$. The formula for $\chi^{\rm SR}$ accounts for that.

Now we integrate $\alpha = \psi$ in the expression for $\tan \chi^{\rm SR}$ for flat space, so we get

$$\tan \chi^{\rm SR}_{\rm flat} = \beta \, \frac{\cos i \cos\psi}{\sin i + \beta \sin\psi}. \tag{63}$$

The total rotation of the PA of both equations, considering the effects of both GR and SR, is

$$\chi^{\rm tot} = \chi^{\rm GR} + \chi^{\rm SR}. \tag{64}$$

2.5 Introducing approximation formula

The real expression is different than simple addition because we need to apply the Lorentz transformation to $\hat{\mathbf{k}}_0$ after taking into account the light-bending effect. Beloborodov (2002) proposed a simple analytical approximation [1]

$$\cos\alpha \approx 1 - (1-u)y \tag{65}$$

where

$$y = 1 - \cos\psi \tag{66}$$

and the lensing factor becomes equal to 1 when we put these expressions in Eq(47) but it only gives accurate results at ψ less than 90 degrees.

Higher accuracy can be achieved by using the proposed relation by Poutanen (2020) [22]. This expression works for a higher inclination

$$\cos\alpha \approx 1 - y(1-u) \left[1 + \frac{u^2 y^2}{112} - \frac{euy}{100} \ln\left(1 - y/2\right) + \frac{y}{2} \right] \tag{67}$$

And we can measure the lensing factor using this expression

$$L \approx 1 + \frac{3u^2y^2}{112} - \frac{e}{100}uy\left[2ln\left(1 - y/2\right) + y\frac{1 - 3y/4}{1 - y/2}\right] \tag{68}$$

Both of these equations help us obtain fast, precise results for the observed parameters of Stokes and the polarized image. To construct polarimetric images on the observer's sky, each photon emitted from the accretion disk is mapped to an impact parameter b that accounts for gravitational light bending in the Schwarzschild metric,

$$b = \frac{r}{\sqrt{1 - u}} \sin\alpha, \tag{69}$$

where $u = R_{\mathrm{S}}/r$ and α is the emission angle. The corresponding sky-plane position angle Φ is then used to determine the orientation of the observed polarization vectors.

Both GR and SR rotation decrease with the increase of inclination, and depolarization is smaller at small inclination. Eq(62) turns

$$\tilde{a} = r + (r - 1)\cos\psi \tag{70}$$

2.6 Results and discussions

By using Beloborodov (2002)[1] approximation for the light bending angle,

$$\cos\alpha = u + (1 - u)\cos\psi \tag{71}$$

which helps us to derive a simple expression for the rotation angle due to light bending

$$\tan\chi^{\mathrm{GR}}_{\mathrm{B02}} \approx \frac{\cos i \sin\varphi}{r\sin i + (r\sin^2 i + \cos^2 i)\cos\varphi} \tag{72}$$

From the general rotation formula of GR, taking the derivative with respect to φ gives us the position of extrema.

$$\cos\varphi^{\mathrm{GR}}_{\mathrm{ext}} = -\frac{r\sin^2 i + \cos^2 i}{r\sin i} \tag{73}$$

In figures 15, 16, and 17, we see χ^{GR} (green line), which shows opposite trends around 0° and 180°. At low inclination, light bending and relativistic effects are quite strong. At low inclination, the disk is visible from outside to the observer due to strong light-bending effects. Matter orbits in an accretion disk, so the direction of the velocity vector relative to the observer keeps changing, and the Lorentz transformation continuously changes the polarization vector. Both GR and SR add to the total polarization vector.

At inclination 30° for $r = 5$, it gives extrema at $\varphi_{\mathrm{ext}} = 180° \pm 34.37°$ where it increases until it reaches a maximum at 145°, and then decreases until 215°, and then starts to increase near the edge of the view.

At higher inclination, GR and SR effects are less strong, as seen from the graphs below. At inclination 50° for $r = 5$, it follows the same trend except $\varphi_{\mathrm{ext}} = 180° \pm 29.08°$.

Again, the same trend is followed here at an inclination of 75°; the extrema are at $\varphi_{\mathrm{ext}} = 180° \pm 14.06°$. From the general equation for χ^{SR}_{flat}, the maximum rotation angle for flat space can be measured

$$\sin\varphi^{\mathrm{SR,\ flat}}_{\mathrm{max}} = -\frac{\beta}{\sin i} \tag{74}$$

And from the general equation for χ_{SR}, the maximum rotation angle for the special theory of relativity can be measured by putting the denominator to zero.

$$\sin\varphi^{\rm SR}_{\rm max} \approx -\frac{\sin^2\zeta}{\beta\sin i\sin\alpha/\sin\psi} \tag{75}$$

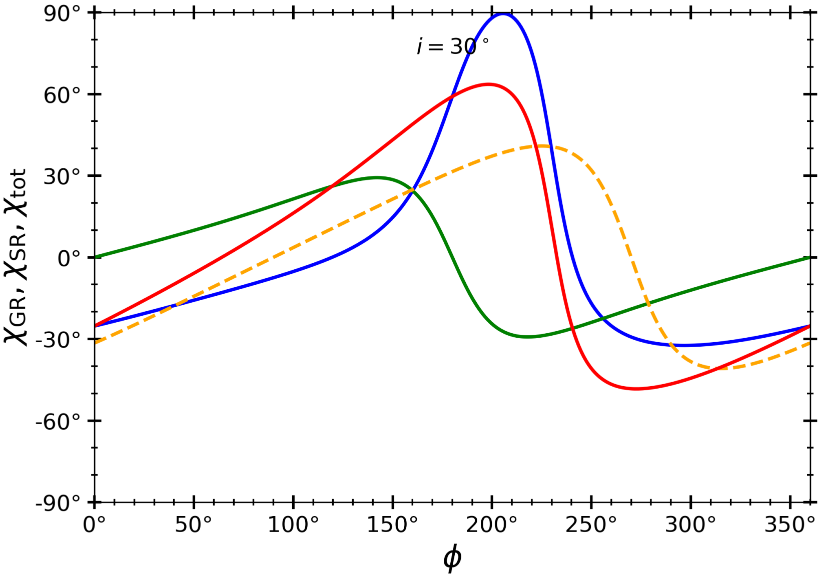

Figure 15: Rotation angles of polarization plane χ_{GR} (represented by green line), χ_{SR} (represented by blue line), χ^{SR}_{flat} (represented by dotted red line), χ_{tot} (represented by red line) for a ring at $r = 5$ at viewing angle $i = 30°$

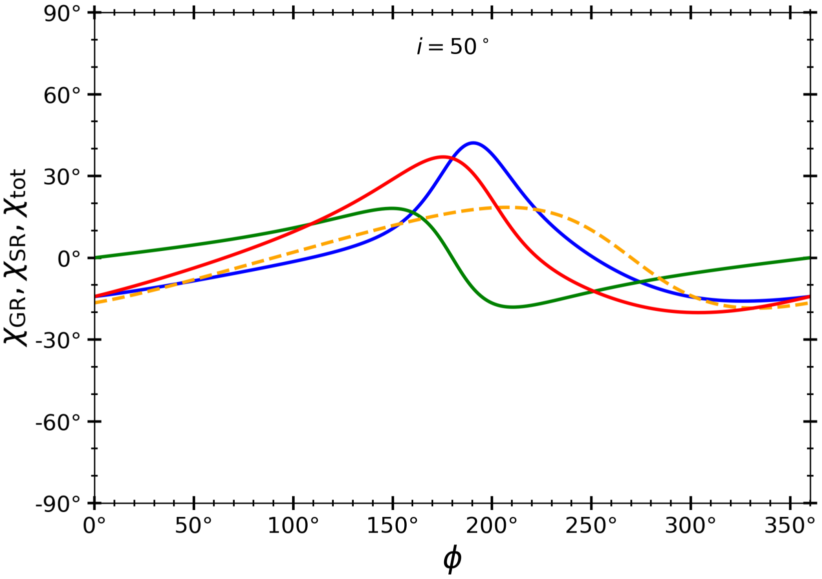

Figure 16: Rotation angles of polarization plane χ_{GR} (represented by green line), χ_{SR} (represented by blue line), χ^{SR}_{flat} (represented by dotted red line), χ_{tot} (represented by red line) for a ring at $r = 5$ at viewing angle $i = 50°$

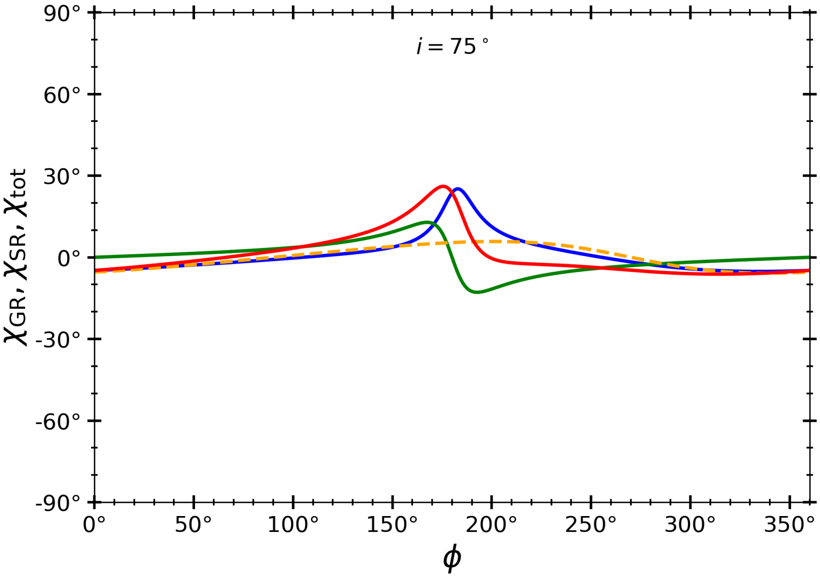

Figure 17: Rotation angles of polarization plane χ_{GR} (represented by green line), χ_{SR} (represented by blue line), χ^{SR}_{flat} (represented by dotted red line), χ_{tot} (represented by red line) for a ring at $r = 5$ at viewing angle $i = 75°$

And by noticing SR rotation will be maximum near the black hole around azimuth 180°, and putting $\psi = 90° + i$, we get

$$\sin \varphi^{\mathrm{SR}}_{\mathrm{max}} \approx -\frac{\cos^2 \alpha \cos i}{\beta \sin i \sin \alpha} \tag{76}$$

χ_{tot} is a combination of both χ_{GR} (light bending) and χ_{SR} (varying Lorentz boost).By using Eq(71) [1] for $r = 5$, the extrema of SR rotation will be $180° \pm 18.21°$ at 30° inclination, and for 50°, it is $180° \pm 12.7°$, while at 75°, it is $180° \pm 4.09°$.

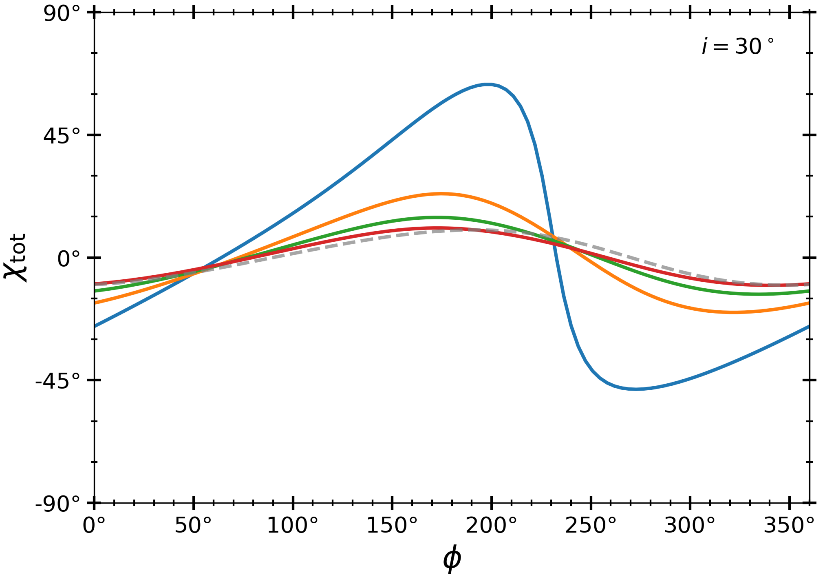

Figure 18: Polarization angle χ_{tot} at $r = 5$ (represented by blue lines), 15 (represented by orange line), 30 (represented by green line), 50 (represented by red line) for angle $i = 30°$ are shown here.

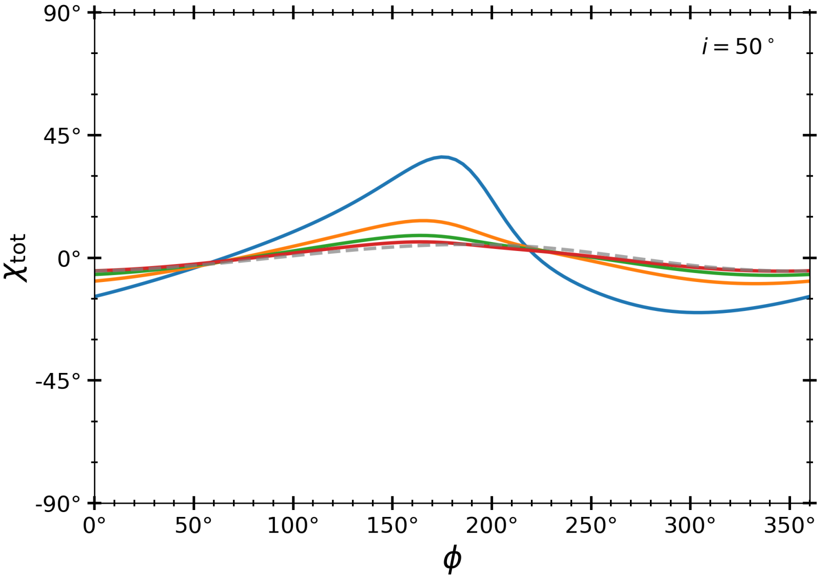

Figure 19: Polarization angle χ_{tot} at $r = 5$ (represented by blue lines), 15 (represented by orange line), 30 (represented by green line), 50 (represented by red line) for angle $i = 50^\circ$ are shown here.

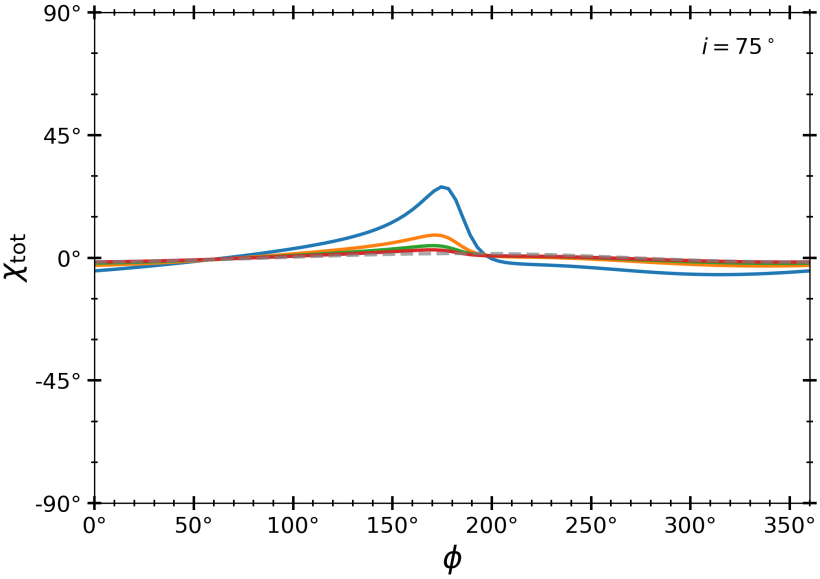

Figure 20: Polarization angle χ_{tot} at $r = 5$ (represented by blue lines), 15 (represented by orange line), 30 (represented by green line), 50 (represented by red line) for angle $i = 75^\circ$ are shown here.

The graphs 18,19,20 show χ_{tot} at different radii and inclinations. As expected, χ_{tot} decreases with the increase of radii. Similarly, the rotation of the polarization angle is maximum at the smaller inclination.

The figures 21, 22, 23 below show the plot between the photon reaching the observer (as the zenith is the angle between the photon propagation direction and the local normal) and the azimuth. At around 180°, photons from behind the disk are visible due to light-bending effects, resulting in the pronounced dips in the graphs around 180°, as these photons lie much closer (above the black hole) than their emission radius. At low and moderate inclination, SR effects dominate the change in ζ', as we are viewing the disk more edge-on.

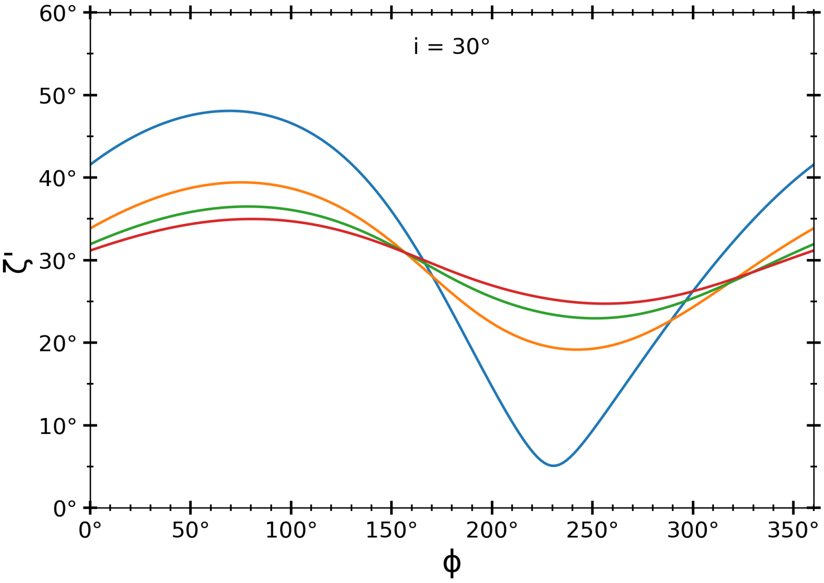

Figure 21: Zenith angle ζ' for $r = 5$ (represented by blue lines), 15 (represented by orange line), 30 (represented by green line), 50 (represented by red line) for angle $i = 30°$ is shown here.

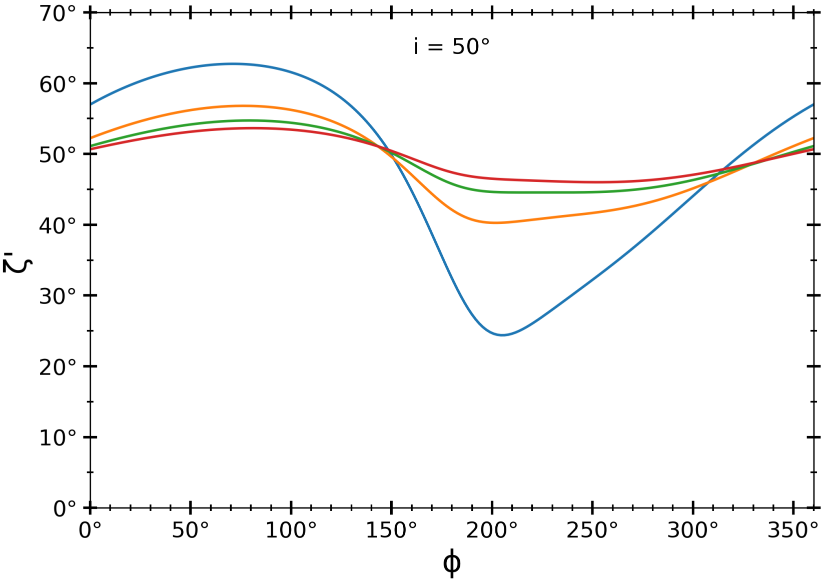

Figure 22: Zenith angle ζ' for $r = 5$ (represented by blue lines), 15 (represented by orange line), 30 (represented by green line), 50 (represented by red line) for angle $i = 50°$ is shown here.

At high inclination, $\zeta' > i$, so the disk is seen more face-on, which results in a high lensing effect as visible from figure 26.

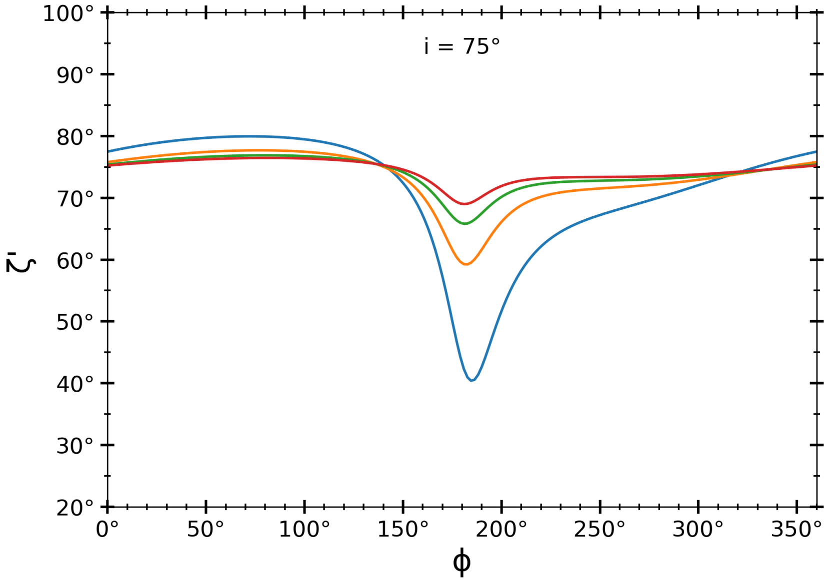

Figure 23: Zenith angle ζ' for $r = 5$ (represented by blue lines), 15 (represented by orange line), 30 (represented by green line), 50 (represented by red line) for angle $i = 75°$ is shown here.

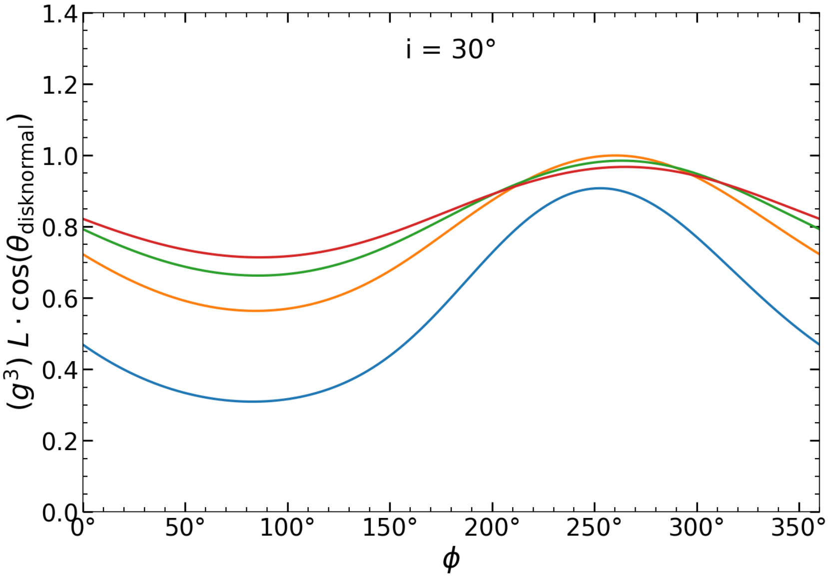

Figure 24: It shows quantity $g^3 L \cos\zeta$ at different radii for $r = 5$ (represented by blue lines), 15 (represented by orange line), 30 (represented by green line), 50 (represented by red line) for angle $i = 30°$.

The graphs 24, 25, 26 show the observed flux $g^3 L \cos\zeta$ as a function of azimuth. At $\phi = 180°$ degrees, the light coming from the far side of the disk (behind the black hole) must pass very close to the compact object to reach the observer and hence experience strong gravitational lensing, which results in increased flux at higher inclination. From the graphs below, the effects of Doppler boosting (where the matter is moving towards the observer) at $\phi > 180°$ and de-boosting (where the matter is moving away from the observer) at $\phi < 180°$ are very apparent, which results in asymmetric azimuthal dependence.

At low inclination, light coming from behind the black hole doesn't add much to the observed flux, and the lensing effects are also less; the velocity component along the line of sight is also smaller, which results in weaker boosting and de-boosting effects compared to high inclination.

To compute the polarization for an optically thick and geometrically thin accretion disk, an electron scattering atmosphere has been assumed [23]. PA is assumed $\chi_0 = \pi/2$; the polarization vector lies perpendicular to the plane, so putting this into the Stokes matrix will give us

$$I'_{E'}(r,\zeta') = I'_{E'}(r,\zeta') \begin{pmatrix} 1 \\ -p_{es}(\zeta') \\ 0 \end{pmatrix} \tag{77}$$

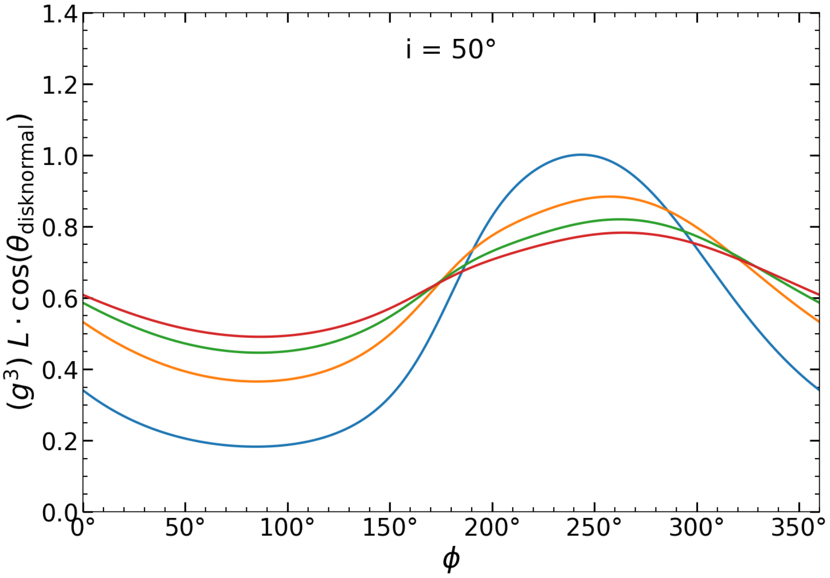

Figure 25: It shows quantity $g^3 L \cos\zeta$ at different radii for $r = 5$ (represented by blue lines), 15 (represented by orange line), 30 (represented by green line), 50 (represented by red line) for angle $i = 50°$.

At high inclination, even though de-boosting effects are stronger, the apparent dip caused by de-boosting is mitigated by lensing, as apparent from Figure 26.

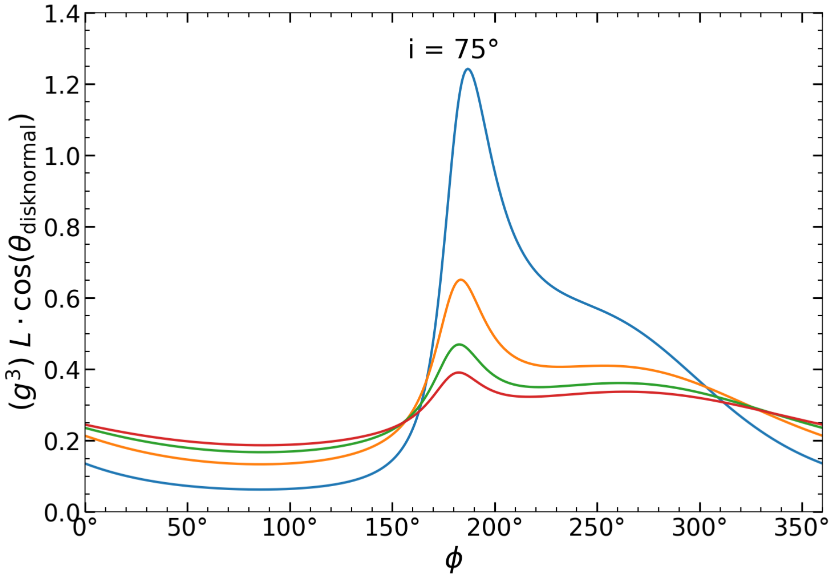

Figure 26: It shows quantity $g^3 L \cos\zeta$ at different radii for $r = 5$ (represented by blue lines), 15 (represented by orange line), 30 (represented by green line), 50 (represented by red line) for angle $i = 75°$.

and thus we obtain the Stokes vector in the fluid frame,

$$I'_{E'}(r,\zeta') = \frac{1}{f_c^4} B_{E'}(T_c(r)) a_{es}(\zeta') \begin{pmatrix} 1 \\ -p_{es}(\zeta') \\ 0 \end{pmatrix} \tag{78}$$

where the angular dependence of outgoing intensity is

$$a_{\mathrm{es}}(\zeta') \approx 0.421 + 0.868 \cos\zeta' \tag{79}$$

and the angular dependence of the polarization vector is

$$p_{\mathrm{es}}(\zeta') \approx 0.1171 \frac{1 - \cos\zeta'}{1 + 3.5\cos\zeta'} \tag{80}$$

$B_{E'}$ is the Planck function of the color temperature, which is given as $T_c = f_c T_{eff}$, $f_c = 1.7$ is the color correction factor, and T_{eff} is the effective temperature which is given by the standard Newtonian disk model [23] as a function of r.

Figure 27 gives us the image of the accretion disk at different inclination angles. At the higher inclination, the light from behind the black hole appears to bend due to the strong lensing effect. The observed spectral flux from the entire disk F_E is obtained by integrating the contributions from the entire disk over radius and azimuth, and then by multiplying the observed spectral vector F_E by $4\pi D^2$, we get the apparent luminosity. By multiplying it by the dimensional photon energy, we get the SED (spectral energy distribution) of radiation emitted by the accretion disk. Through this scaling/normalization, we get rid of M and $\dot{M}$ from the spectra.

$$T^4_{eff}(r) = \frac{3GM\dot{M}}{8\pi\sigma_{SB}R^3}\left(1 - \sqrt{\frac{3R_S}{R}}\right) = T^4_* t^4(u) \tag{81}$$

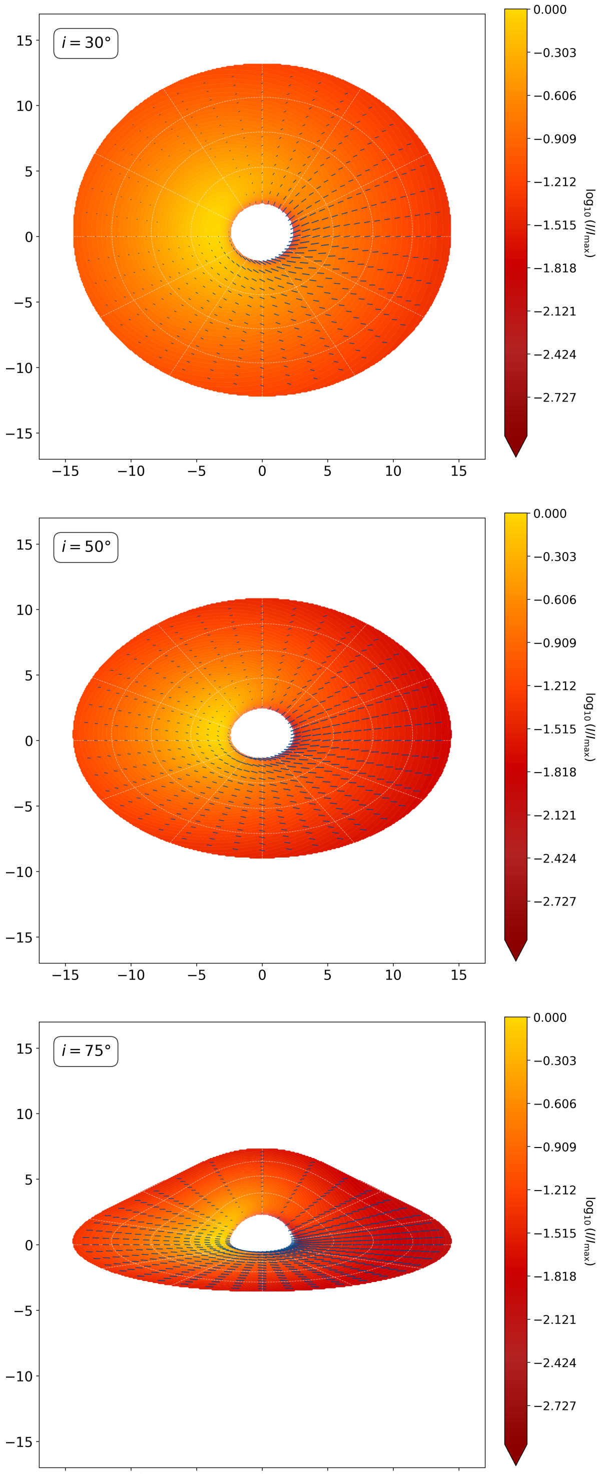

Figure 27: The accretion disk image is observed at three different angles. The color represents bolometric intensity $g^4\, t^4(u)\, a_{\rm es}(\zeta')$; blue lines are showing polarization; coordinates on the sky are in units of R_s; black contour shows lines of rings at equal azimuth and equal radius.

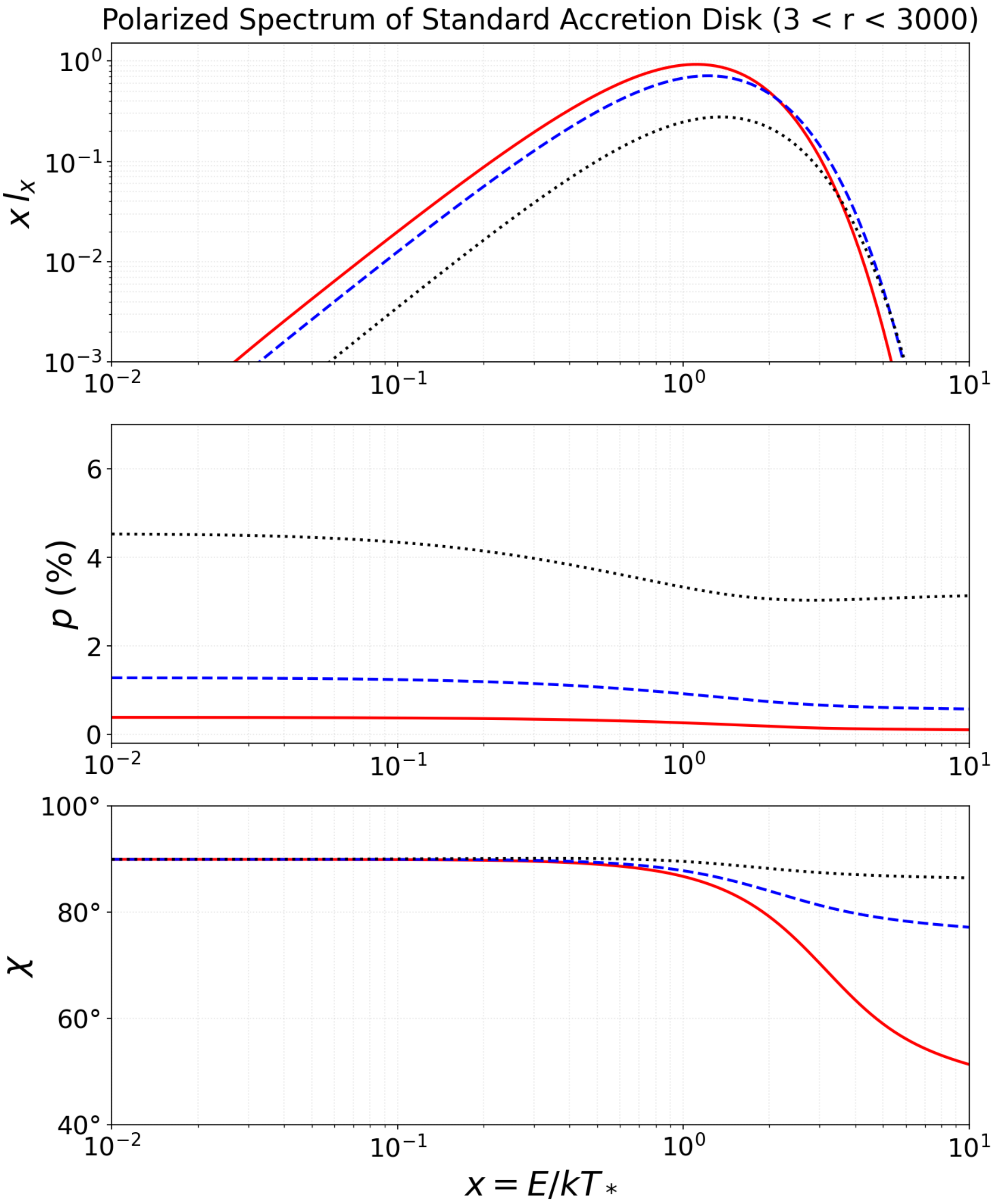

Figure 28: (a) shows luminosity, (b) is for polarization degree, and (c) is for polarization degree on the y-axis. Photon energy is on the x-axis, red solid lines show inclination 30°, blue dotted lines represent inclination 60°, and inclination 75° is shown by black dotted lines.

where

$$T_*^4 = \frac{3GM\dot{M}}{8\pi\sigma_{\mathrm{SB}}R_S^3} \tag{82}$$

$$t(u) = \left[u^3\left(1-\sqrt{3u}\right)\right]^{1/4} \tag{83}$$

$$xl_x = \frac{xL_x}{\sigma_{SB} T_*^4 R_S^2} = \frac{60}{\pi^4}\int_{r_{in}}^{r_{out}} \frac{r\,dr}{\sqrt{1-u}} \int_0^{2\pi} d\varphi \frac{g^4}{f_c^4}\mathcal{L}\cos\zeta \times \left[\frac{x'^4 a_{es}(\zeta')}{e^{x'/f_c t(u)}-1}\begin{pmatrix}1\\ p_{es}(\zeta')\cos(2[\chi^{tot}+\chi_0])\\ p_{es}(\zeta')\sin(2[\chi^{tot}+\chi_0])\end{pmatrix}\right] \tag{84}$$

Figure 28 shows that luminosity is highest at low inclinations because the observer's line of sight is closer to normal at low inclinations. Due to the Doppler effect, the graph shifts to higher energy at high inclination.

Then we can calculate PD

$$p(x) = \frac{\sqrt{I_{x,Q}^2 + I_{x,U}^2}}{I_{x,I}} \tag{85}$$

and PA

$$\chi(x) = \frac{1}{2}\arg(I_{x,Q} + iI_{x,U}) \tag{86}$$

$$F_E = \frac{R_S^2}{D^2}\int_{r_{\rm in}}^{r_{\rm out}}\int_0^{2\pi} g^3 L \cos\zeta\, I'_E(\zeta')\, d\Omega \tag{87}$$

As seen from Figure 28, polarization is higher at higher inclination, and depolarization effects are only important at higher energies because emission from inner radii becomes important at high energies.

3 Conclusion and limitations

In this work, the analytical method developed by Loktev [27] is adopted to study the variation of light polarization with observer inclination. The original method provides explicit analytical expressions for the rotation of the polarization plane, accurately capturing the effects of both gravitational light bending and relativistic aberration. These expressions enable efficient and precise computation of emission angles, flux, and polarization without the need for time-consuming ray tracing.

We apply our method to three viewing angles, 30°, 60°, and 75°, to examine how the polarization pattern varies across the disk. This approach is fully analytical and helps us create faster, accurate, and detailed polarimetric graphs . Although we did not derive new formulas, we used only the expressions derived in the Loktev paper[27]. Generated polarimetric graphs clearly show how strongly the observed polarization depends on the observer's viewing angle. Overall, the results illustrate the impact of strong gravity on polarization signatures and provide a practical way to interpret polarimetric observations of compact objects

However, in this paper, the analytical model has been simplified. We assumed an optically thick, plane-parallel electron scattering disk, which made our calculation of the strokes vector easier because, by considering this, only two components of the strokes vector were left non-zero. However, measurements of real astrophysical systems can differ substantially. For example, in black hole systems with low accretion rates, the surrounding flow is often optically thin. In these cases, low-energy emission comes from synchrotron radiation produced by relativistic electrons moving through magnetic fields. For supermassive black holes, this emission typically appears at radio to submillimeter wavelengths, while in X-ray binaries it is seen at optical to infrared wavelengths. The magnetic fields responsible for this emission are often not aligned with the disk normal. In these scenarios, the Stokes vector includes additional components (U and possibly V), and the polarization properties can deviate substantially from those assumed in our model. Nevertheless, these changes affect only the local Stokes parameters, while the overall computational scheme for the observed Stokes vector, including polarization angle rotation, remains valid.

The model assumes that the gas has purely azimuthal motion. In reality, particularly in low-accretion-rate, optically thin flows (such as those observed in M87 by the EHT), the radial velocity component may be significant. While general relativistic rotation of the polarization plane due to light bending is independent of the velocity field, special relativistic effects (such as aberration and Doppler boosting) require a more general vector treatment to accurately compute polarization rotation. The formalism assumes emission originates from a smooth, extended disk. In practice, emission may be localized in small co-rotating "hot spots." In such cases, light travel time delays become important, as the photon arrival time depends on the spot's orbital phase. This modifies the relationship between the emission azimuth and the observed Stokes vector and requires adjustments in the integration over the emission region.

3.1 Future Work

Future work could include many improvements; for example, the model could extend the analytical techniques developed here to Kerr black holes, incorporating black hole spin and frame-dragging effects. Predictions of Polarization signatures can be improved by experimenting with more realistic accretion-flow geometries, including optically thin and geometrically thick flows, and complex magnetic field configurations. Time-dependent effects, such as orbiting hot spots and turbulence, would also help in the modeling of variable polarization signals. Multiwavelength polarimetry and comparisons with GRMHD simulations can further validate and refine the models. These improvements can make the model more suitable for real observations for the upcoming missions.

References

[1] Andrei M. Beloborodov. "Gravitational Bending of Light Near Compact Objects". In: *The Astrophysical Journal* 566.2 (2002), pp. L85–L88. DOI: `10.1086/339511`.

[2] S. Chandrasekhar. "The stability of non-dissipative Couette flow in hydromagnetics". In: *Proceedings of the National Academy of Sciences* 46.2 (1960), pp. 253–257.

[3] Tanmoy Chattopadhyay, Abhay Kumar, A. R. Rao, et al. "High Hard X-Ray Polarization in Cygnus X-1 Confined to the Intermediate Hard State: Evidence for a Variable Jet Component". In: *The Astrophysical Journal Letters* 960.1 (2023), p. L2. DOI: `10.3847/2041-8213/ad118d`.

[4] Maxime Chauvin et al. "Accretion geometry of the black-hole binary Cygnus X-1 from X-ray polarimetry". In: *Nature Astronomy* 2.8 (2018), pp. 652–655. DOI: `10.1038/s41550-018-0489-x`.

[5] Maxime Chauvin et al. "PoGO+ polarimetric constraint on the synchrotron jet emission of Cygnus X-1". In: *Monthly Notices of the Royal Astronomical Society: Letters* 483.1 (2018), pp. L138–L143. DOI: `10.1093/mnrasl/sly233`.

[6] Paul A. Connors, Tsvi Piran, and Richard F. Stark. "Polarization features of X-ray radiation emitted near black holes". In: *Astrophysical Journal* 235 (1980), pp. 224–244.

[7] Chris Done, Marek Gierliński, and Aya Kubota. "Modelling the behaviour of accretion flows in X-ray binaries: Everything you always wanted to know about accretion but were afraid to ask". In: *The Astronomy and Astrophysics Review* 15.1 (2007), pp. 1–66.

[8] M. Dovčiak, V. Karas, and G. Matt. "Polarization signatures of strong gravity in active galactic nuclei accretion discs". In: *Monthly Notices of the Royal Astronomical Society* 355.3 (2004), pp. 1005–1009.

[9] M. Dovčiak et al. "Light-bending scenario for accreting black holes in X-ray polarimetry". In: *The Astrophysical Journal* 731.1 (2011), p. 75.

[10] M. Dovčiak et al. "Thermal disc emission from a rotating black hole: X-ray polarization signatures". In: *Monthly Notices of the Royal Astronomical Society* 391.1 (2008), pp. 32–38.

[11] Marek Gierliński et al. "Radiation mechanisms and geometry of Cygnus X-1 in the soft state". In: *Monthly Notices of the Royal Astronomical Society* 309.2 (1999), pp. 496–512. DOI: `10.1046/j.1365-8711.1999.02875.x`.

[12] J. Horák and V. Karas. "On the role of strong gravity in polarization from scattering of light in relativistic flows". In: *Monthly Notices of the Royal Astronomical Society* 365.3 (2006), pp. 813–826.

[13] E. Jourdain et al. "Separation of two contributions to the high energy emission of Cygnus X-1: Polarization measurements with INTEGRAL/SPI". In: *The Astrophysical Journal* 761.1 (2012), p. 27. DOI: `10.1088/0004-637x/761/1/27`.

[14] Andreas Kipf et al. *LSI: A Learned Secondary Index Structure.* 2022. arXiv: `2205.05769 [cs.DB]`. URL: `https://arxiv.org/abs/2205.05769`.

[15] Henric Krawczynski et al. "Polarized x-rays constrain the disk-jet geometry in the black hole x-ray binary Cygnus X-1". In: *arXiv preprint arXiv:2306.15438* (2023). URL: `https://arxiv.org/abs/2306.15438`.

[16] P. Laurent et al. "Polarized Gamma-Ray Emission from the Galactic Black Hole Cygnus X-1". In: *Science* 332.6028 (2011), pp. 438–439. DOI: `10.1126/science.1200848`.

[17] K. S. Long and et al. "Observations of Cyg X-1 with the HEAO-1 A-2 experiment". In: *Astrophysical Journal* 238 (1980), p. 710.

[18] D. I. Nagirner and J. Poutanen. "Single Compton scattering". In: *Astronomy Reports* 9 (1994).

[19] Ramesh Narayan and Insu Yi. "Advection-dominated Accretion: Underfed Black Holes and Neutron Stars". In: *The Astrophysical Journal* 452 (1995), p. 710. DOI: `10.1086/176343`.

[20] Ramesh Narayan and Insu Yi. "Advection-dominated accretion: underfed black holes and neutron stars". In: *arXiv preprint astro-ph/9411059* (1994).

[21] Scott C. Noble, Julian H. Krolik, and John F. Hawley. "Dependence of Inner Accretion Disk Stress on Parameters: The Schwarzschild Case". In: *The Astrophysical Journal* 711.2 (2010), pp. 959–973. DOI: `10.1088/0004-637X/711/2/959`.

[22] Juri Poutanen. "Accurate analytic formula for light bending in Schwarzschild metric". In: *Astronomy & Astrophysics* 640 (2020), A24.

[23] N. I. Shakura and R. A. Sunyaev. "Black holes in binary systems. Observational appearance." In: *Astronomy & Astrophysics* 24 (1973), pp. 337–355.

[24] Stuart L. Shapiro, Alan P. Lightman, and Douglas M. Eardley. "A two-temperature accretion disk model for Cygnus X-1-Structure and spectrum". In: *Astrophysical Journal* 204 (1976), pp. 187–199.

[25] R. F. Stark and P. A. Connors. "Observational test for the existence of a rotating black hole in CYG X-1". In: *Nature* 266.5601 (1977), pp. 429–430.

[26] James F. Steiner et al. *An IXPE-Led X-ray Spectro-Polarimetric Campaign on the Soft State of Cygnus X-1: X-ray Polarimetric Evidence for Strong Gravitational Lensing.* 2024. arXiv: `2406.12014 [astro-ph.HE]`. URL: `https://arxiv.org/abs/2406.12014`.

[27] Alexandra Veledina et al. "Astronomical puzzle Cyg X-3 is a hidden Galactic ultraluminous X-ray source". In: *Nature Astronomy* (2023), arXiv:2303.01174. DOI: `10.48550/arXiv.2303.01174`.

[28] Feng Yuan. "Luminous hot accretion flows: thermal equilibrium curve and thermal stability". In: *The Astrophysical Journal* 594.2 (2003), p. L99.

[29] Andrzej A. Zdziarski and Marek Gierliński. "Radiative Processes, Spectral States and Variability of Black-Hole Binaries". In: *Progress of Theoretical Physics Supplement* 155 (2004), pp. 99–119. DOI: `10.1143/ptps.155.99`.